

Connecting *JWST* discovered N/O-enhanced galaxies to globular clusters: Evidence from chemical imprints

Xihan Ji,^{1,2}★ Vasily Belokurov,³ Roberto Maiolino,^{1,2,4} Stephanie Monty,³ Yuki Isobe,^{1,2,5} Andrey Kravtsov,^{6,7,8} William McClymont,^{1,2} Hannah Übler⁹

¹*Kavli Institute for Cosmology, University of Cambridge, Madingley Road, Cambridge, CB3 0HA, UK*

²*Cavendish Laboratory, University of Cambridge, 19 JJ Thomson Avenue, Cambridge, CB3 0HE, UK*

³*Institute of Astronomy, University of Cambridge, Madingley Road, Cambridge CB3 0HA, UK*

⁴*Department of Physics and Astronomy, University College London, Gower Street, London WC1E 6BT, UK*

⁵*Waseda Research Institute for Science and Engineering, Faculty of Science and Engineering, Waseda University, 3-4-1, Okubo, Shinjuku, Tokyo 169-8555, Japan*

⁶*Department of Astronomy and Astrophysics, The University of Chicago, Chicago, IL 60637 USA*

⁷*Kavli Institute for Cosmological Physics, The University of Chicago, Chicago, IL 60637 USA*

⁸*Enrico Fermi Institute, The University of Chicago, Chicago, IL 60637 USA*

⁹*Max-Planck-Institut für extraterrestrische Physik, Gießenbachstraße 1, 85748 Garching*

26 November 2025

ABSTRACT

Recent *JWST* observations have revealed a growing population of galaxies at $z > 4$ with elevated nitrogen-to-oxygen ratios. These “N/O-enhanced” galaxies (NOEGs) exhibit near- to super-solar N/O at sub-solar O/H, clearly deviating from the well-established scaling relation between N/O and O/H observed in local galaxies. The origin of this abundance anomaly is unclear. Interestingly, local globular clusters also exhibit anomalous light-element abundances, whose origin remains debated. In this work, we compare the chemical abundance patterns of 22 known NOEGs at $0 \lesssim z \lesssim 12$ – primarily discovered with *JWST* – to those observed in local globular clusters. We find similarities in the abundances of C, N, O, Fe, and He between the two populations. The similar abundance patterns support the scenario in which globular cluster stars formed within proto-cluster environments – similar to those traced by NOEGs – that were self-enriched. Indeed, the enhancement in N/O in early galaxies appears to be only found in dense stellar environments with $\Sigma_{\star} \gtrsim 10^{2.5} M_{\odot} \text{ pc}^{-2}$, as expected for the progenitors of globular clusters in the Milky Way, and similar to those of star clusters identified in strongly lensed high-redshift galaxies. Furthermore, we find a tentative positive correlation between N/O ratios and stellar mass among NOEGs. The apparent high occurrence rate of NOEGs at high redshift is consistent with the picture of cluster-dominated star formation during the early stages of galaxy evolution. Measuring chemical abundances across diverse stellar environments in high-redshift galaxies will be crucial for elucidating the connection between NOEGs and globular clusters.

Key words: galaxies: abundances – galaxies: high-redshift – Galaxy: globular clusters: general

1 INTRODUCTION

Chemical enrichment is an essential part of galaxy evolution, which is closely related to the baryonic cycle inside and outside of galaxies (Maiolino & Mannucci 2019; Kobayashi et al. 2020). With observations of local galaxies and stars, abundances of elements such as oxygen, nitrogen, carbon, iron, helium, and so forth have been routinely measured on galactic and sub-galactic scales in statistical samples. Notably, observational studies of galaxies in the local Universe show there exist tight correlations between elemental abundance ratios such as N/O, C/O, and O/H in the interstellar medium (ISM) as well as stellar atmospheres, spanning more than one order of magnitude in these abundances (e.g., Vila-Costas & Edmunds 1993; Andrews & Martini 2013; Belfiore et al. 2017; Nicholls et al. 2017).

The observed correlations imply a standard path for chemical evolution, and current chemical evolution models can well reproduce the observed abundances (e.g., Vincenzo et al. 2016), although there is still debate on the details of the enrichment processes (Matteucci 2021). Based on current chemical evolution models, the relation between N/O and O/H can be interpreted as a combination of two enrichment channels. More specifically, nitrogen synthesis in stars proceeds through the CNO cycle, which relies on trace carbon and oxygen nuclei as catalysts; it is the origin of those catalysts, as well as the stellar layer where they are recycled, that divides nitrogen production into two distinct regimes, which are primary and secondary productions. Low-metallicity massive (and/or fast-rotating) stars produce primary nitrogen at the early time of galaxy evolution, when freshly synthesized C and O from the He-burning core are mixed down into the adjacent H-burning shell; there the CNO cycle converts them to ^{14}N , and core-collapse supernovae expel this metal-independent yield. By adjusting the yield of primary N from massive

★ E-mail: xj274@cam.ac.uk

stars, chemical evolution models can reproduce the well-known constant N/O “plateau” at low O/H (see [Matteucci 1986](#); [Henry et al. 2000](#); [Prantzos et al. 2018](#); [Kobayashi et al. 2020](#)). Intermediate-mass asymptotic giant branch (AGB) stars, on the other hand, produce both primary and secondary nitrogen. Here secondary N is made through CNO cycling of the preexisting C and O inherited from the birth cloud, at the base of the convective envelope reaching temperatures of $\gtrsim 50$ MK (hot-bottom burning). Primary N is made from C made in the interior by the triple- α process and “dredged up” to the hot-bottom burning region. Since the seed C and O now reflect the star’s initial metallicity, the secondary yield scales with O/H, which, combined with the potential differential outflows at high O/H, driving the observed rise in N/O at higher metallicity with a typical delay time of 0.1 - 1 Gyr (e.g., [Meynet & Maeder 2002](#); [Vincenzo et al. 2016](#); [Maiolino & Mannucci 2019](#)). These primary and secondary channels successfully reproduce the N/O–O/H trend in nearby galaxies.

Expanding on this established picture requires probing elemental abundances across cosmic time, particularly in the early Universe, where the physical conditions and enrichment pathways may diverge significantly from those in the local galaxy population. However, the observational constraints on elemental abundances in the early Universe are more difficult due to the redshift of spectral features typically used to make abundance measurements (e.g., $[\text{O III}]\lambda 5007$ goes to $> 2 \mu\text{m}$ at $z > 3$). In recent years, thanks to the sensitivity and wavelength coverage of *JWST* and its instruments, especially the Near Infrared Spectrograph (NIRSpec, [Jakobsen et al. 2022](#); [Böker et al. 2023](#)), elemental abundances have been estimated for galaxies even close to cosmic dawn, i.e. up to $z > 10$ (e.g., [Bunker et al. 2023](#); [Cameron et al. 2023](#); [Castellano et al. 2024](#); [Napolitano et al. 2025](#); [Carniani et al. 2025](#); [Schouws et al. 2025](#)). These *JWST* observations have revealed a puzzling population of “chemically abnormal” galaxies at high redshift, which show unexpectedly bright nitrogen emission lines indicative of super-solar abundance ratios of N/O at sub-solar O/H, in contrast to the significantly sub-solar N/O ratios seen in metal-poor galaxies in the local Universe. A number of these galaxies are found at $z \gtrsim 6$, meaning that if the measured abundances are interpreted as a result of global chemical evolution, their cosmic age is even less than the typical delay time of significant nitrogen enrichment by intermediate-mass AGB stars (~ 1 Gyr) according to standard chemical evolution models. Still, while galaxy-integrated N/O upturns often appear on Gyr scales, the onset of AGB hot-bottom-burning N production is much earlier: massive/intermediate-mass AGBs ($\sim 3.5 - 8 M_{\odot}$) eject N-rich winds from $\sim 30 - 40$ Myr after birth and largely cease by ~ 300 Myr. Thus, in principle, AGB-wind N pollution is plausible even at $z \gtrsim 6$ ([D’Antona et al. 2023](#)).

While such “N/O enhanced” galaxies (hereafter NOEGs) were identified in the pre-*JWST* era – mainly among quasars ($\sim 1\%$ of QSOs at $1.6 \leq z \leq 4$; [Bentz & Osmer 2004](#); [Bentz et al. 2004](#); [Jiang et al. 2008](#)), where they were speculated to reflect super-solar metallicities in broad-line regions ([Hamann & Ferland 1999](#)) – they were very rare in local star-forming (SF) galaxies ([James et al. 2009](#)). Only now, with *JWST*, has strong N/O enhancement been confirmed in statistical samples of metal-poor galaxies at high redshift.

Thus far, there are more than 20 galaxies with established N/O enhancement at $z > 2$, and there are potentially more NOEGs missing due to the wavelength coverage and depths of current *JWST* observations ([Hayes et al. 2025](#); [Isobe et al. 2023, 2025b](#)). Standard chemical evolution models fail to explain the nitrogen enhancement in NOEGs, and alternative enrichment channels such as fast-rotating massive stars, very massive stars (VMS; $M_{\star} > 100 M_{\odot}$), extremely massive stars (EMSS; $10^3 M_{\odot} < M_{\star} < 10^4 M_{\odot}$), super massive

stars (SMSs; $M_{\star} > 10^4 M_{\odot}$), Wolf-Rayet (WR) stars with direct collapses, tidal disruption events (TDEs), early enrichment of AGB stars (combined with inflows and/or differential outflows), and so forth, have been proposed ([Tsiatsiou et al. 2024](#); [Vink 2023](#); [Gieles et al. 2025](#); [Nagele & Umeda 2023](#); [Charbonnel et al. 2023](#); [Nandal et al. 2024a,b, 2025](#); [Watanabe et al. 2024](#); [Cameron et al. 2023](#); [D’Antona et al. 2023](#); [Rizzuti et al. 2025](#); [McClymont et al. 2025a](#)) Still, the exact enrichment mechanism remains poorly constrained.

The abundance of NOEGs found at high redshift raises a key question of whether we can see the relics of these systems in the local Universe. If the gas showing abnormal abundances at high redshift later formed stars, one might expect to observe such abundance patterns in certain populations of old stars. Interestingly, it has been known for a long time that stars in globular clusters (GCs) of the Milky Way (MW) exhibit peculiar abundances in light elements, including He, C, N, O, Na, Mg, Al, and so forth ([Gratton et al. 2004](#)). In addition, many of these GCs are estimated to have formed at $z > 4$ (e.g., [VandenBerg et al. 2013](#)), which coincides with the redshift of NOEGs that are still actively forming stars at the time of *JWST* observations. It has been suggested that the deep gravitational potentials of proto-GCs had allowed them to imprint the anomalous chemical abundances in their stars. Observations of local GCs have revealed a spread of chemical abundances related to the multiple populations of stars (e.g., [Smith 1987](#); [Kraft 1994](#); [Gratton et al. 2001](#), and references therein). Traditionally, stars in GCs have been split into two generations, those with light element abundances similar to MW field stars at the same iron abundances (1G), and those with enhanced N, Na, and depleted O (2G) (see [Bastian & Lardo 2018](#); [Gratton et al. 2019](#); [Milone & Marino 2022](#), for recent reviews on the subject). Depending on the mass of the cluster, light-element anomalies may extend to an enhancement in Al and depletion in Mg, and, in extreme cases, an enhancement in K (e.g., in the massive GCs, NGC 2419, NGC 2808, NGC 5139, and NGC 4833; [Cohen & Kirby 2012](#); [Mucciarelli et al. 2012, 2015](#); [Mészáros et al. 2020](#); [Carretta 2021](#)). Importantly, the fraction of chemically peculiar stars in a GC strongly correlates with the cluster mass (see e.g., [Milone et al. 2017, 2018](#); [Bastian & Lardo 2018](#); [Gratton et al. 2019](#)). This correlation is noticeably tighter if the cluster’s initial (i.e., before evaporation and tidal shredding) mass is considered (see e.g., Figures 6 and 4 in [Gratton et al. 2019](#); [Belokurov & Kravtsov 2023](#), respectively). While the nucleosynthetic site is debated, these anomalies are clear evidence of the CNO cycle, NeNa and MgAl chains operating at ever-increasing temperatures between the formation of 1G and 2G stars. Suggested sites have included WR stars, AGB stars ([Ventura et al. 2001](#); [D’Antona et al. 2023](#); [McClymont et al. 2025a](#)), fast-rotating massive stars (see e.g., [Maeder & Meynet 2006](#); [Prantzos & Charbonnel 2006](#)), interactive massive binaries ([de Mink et al. 2009](#)), very massive stars (VMSs, see e.g., [Vink 2018](#)), super-massive stars (SMSs, see e.g., [Denissenkov & Hartwick 2014](#); [Prantzos et al. 2017](#)). Also, extremely massive stars (EMSS, [Gieles et al. 2025](#)) and AGB stars ([Ventura et al. 2013, 2018](#); [Alvarez Garay et al. 2024](#)) have been shown to explain the exceptionally high N abundances *and* to achieve temperatures high enough to reach the MgAl chain in massive GCs.

Given the close resemblance of the two unsolved problems in the chemical enrichment of NOEGs and GCs, some recent works have suggested that NOEGs discovered by *JWST* host proto-GCs and thus the two problems are interconnected (e.g., [Belokurov & Kravtsov 2023](#); [Isobe et al. 2023](#); [Senchyna et al. 2024](#); [Marques-Chaves et al. 2024](#); [Gieles et al. 2025](#); [Renzini 2025](#)). Indeed, recent *JWST* observations have hinted that NOEGs are likely more compact than normal star-forming galaxies at similar redshift, implying that star formation in these systems occurs in dense, spatially concentrated

regions (e.g., [Topping et al. 2024](#); [Schaerer et al. 2024](#); [Harikane et al. 2025](#)). For example, in the gravitationally lensed galaxy, Sunburst Arc at $z = 2.26$, where several star clusters are spatially separated, it has been shown that the nitrogen enhancement occurs in a Lyman-continuum leaking “super star cluster” (LyC, [Pascale et al. 2023](#)), but not seen in the integrated spectrum of the galaxy ([Welch et al. 2025](#)). Such young, compact and extremely massive (age $\lesssim 4$ Myr, $R_e \lesssim 20$ pc, $M_\star \sim 10^7 M_\odot$) super star clusters are very rare in the local Universe but their lower-mass analogs have been spotted in extreme starbursts and dramatic, gas-rich mergers ([Portegies Zwart et al. 2010](#)).

More recently, [Isobe et al. \(2025b\)](#) show that nitrogen enhancement in *JWST*-observed galaxies is correlated with high gas densities and presence of active galactic nuclei (AGN), which indicate a connection between proto-GC formation and black hole seeding through VMSs/EMSs/SMSs and/or runaway merging. In the early Universe, it is expected that star formation is bursty ([Caplar & Tacchella 2019](#); [Tacchella et al. 2020](#); [Sun et al. 2023](#); [Kravtsov & Belokurov 2024](#); [McClymont et al. 2025b](#)) and mostly contributed by clumpy components manifested as massive stellar clusters, whereas more smooth, disk-dominated star formation only becomes prevalent at a later epoch (e.g., [Yu et al. 2021, 2023](#); [Hafen et al. 2022](#); [Dillamore et al. 2024](#); [Semenov et al. 2025](#)). In this picture, if the “chemical anomaly” is a natural outcome of proto-cluster evolution, nitrogen enhancement is expected to be more common in the early Universe, when star formation is bursty and before the emergence of dynamically stable stellar disks. Recent simulations point to a characteristic mass scale around $10^{11} M_\odot$ in halo mass or a few $\times 10^9 M_\odot$ in stellar mass, above which long-lived, kinematically cold disks emerge (e.g., [Dillamore et al. 2024](#); [Semenov et al. 2025](#)). If a galaxy’s dynamical state is linked to its ability to form massive star clusters, then anomalously high N/O should be found preferentially in systems below this threshold, and it is more likely to happen in the early Universe.

Thus far, however, there has yet to be a systematic comparison between the chemical imprints of stars in GCs and ISM in NOEGs to assess this connection. In this work, we compiled a sample of 21 NOEGs at $z > 2$ together with a local analog of high- z NOEGs, Mrk 996. Our aim is to compare the measured chemical abundance patterns of these systems with MW stars, especially those identified in GCs, and investigate whether NOEGs can host progenitors of GCs observed today, if we assume MW GCs are representative.

The structure of this manuscript is as follows. In Section 2, we introduce our sample galaxies and stars as well as the relevant observations. In Section 3, we describe derivations of the physical properties of these sources. In Section 4, we compare the derived abundance patterns of NOEGs and MW GCs. We discuss the connection between NOEGs and MW GCs as well as the validity of NOEG identifications in Section 5, and we draw our conclusions in Section 6. Throughout this work, we assume a flat Λ CDM cosmology with $h = 0.674$ and $\Omega_m = 0.315$ ([Planck Collaboration et al. 2020](#)). We adopt the solar abundance set from [Lodders \(2021\)](#), with $12 + \log(\text{He/H})_\odot = 10.924$, $12 + \log(\text{C/H})_\odot = 8.47$, $12 + \log(\text{N/H})_\odot = 7.85$, $12 + \log(\text{O/H})_\odot = 8.71$, and $12 + \log(\text{Fe/H})_\odot = 7.48$. We follow the convention of the nebular community by referring to the relative oxygen abundance, O/H, as the metallicity, unless otherwise specified.

2 OBSERVATIONAL DATA

In this section, we describe the observational data we used, including those of galaxies and stars. All sources are drawn from existing publications.

2.1 N/O-enhanced galaxies

We compiled a sample of 21 NOEGs at $2 \lesssim z \lesssim 12$ in the literature, corresponding to a range of cosmic ages of 350 Myr - 2.8 Gyr after the Big Bang ([Pascale et al. 2023](#); [Labbé et al. 2024](#); [Ji et al. 2024](#); [Cameron et al. 2023, 2024](#); [Topping et al. 2024](#); [Isobe et al. 2023](#); [Schaerer et al. 2024](#); [Curti et al. 2025](#); [Napolitano et al. 2025](#); [Bunker et al. 2023](#); [Castellano et al. 2024](#); [Navarro-Carrera et al. 2024](#); [Arellano-Córdova et al. 2025](#); [Stiavelli et al. 2025](#)). These sources are all reported to have $(\text{N/O}) \gtrsim (\text{N/O})_\odot$ at $(\text{O/H}) < (\text{O/H})_\odot$. We emphasize that the NOEGs are selected from parent samples with different depths and complex selection functions. Thus, our aim is not to quantify, for example, the actual fraction of NOEGs in early galaxies and the relevant statistical interpretations, but rather understand whether the NOEGs, as a potentially distinct population of early galaxies, exhibit any connections to the local relics. Spectroscopic observations that confirm nitrogen enhancement in these sources were primarily made via *JWST*/NIRSpec except for the Lyman continuum (LyC) leaking super star cluster in the gravitationally lensed Sunburst Arc at $z = 2.37$, whose chemical abundances were derived from observations via the ground-based Very Large Telescope (VLT) with MUSE integral field unit (IFU) and X-shooter spectroscopy in addition to *JWST*/NIRSpec ([Pascale et al. 2023](#); [Welch et al. 2025](#)). In addition to these high- z NOEGs, we include a blue compact dwarf (BCD) galaxy, Mrk 996, at $z \sim 0$, which shows nitrogen enhancement with respect to the local relation of N/O-O/H via VLT VIMOS observations and is a rare local analog of NOEGs at high redshift ([James et al. 2009](#)). We refer the readers to the sources we listed for details of data reduction and emission-line measurements. We summarize some derived properties for these sources in Table 1, including redshift, stellar mass, and effective radius. Figure 1 shows comparisons between the stellar masses, sizes, and redshifts of NOEGs and those derived photometrically for *JWST*-observed galaxies at $5 < z_{\text{photo}} < 14$ by [Morishita et al. \(2024\)](#) as well as at $3 < z_{\text{photo}} < 9$ in the *JWST* Advanced Deep Extragalactic Survey (JADES, [Bunker et al. 2024](#); [Eisenstein et al. 2023a,b](#); [D’Eugenio et al. 2025](#)). Overall, the high- z NOEGs show relatively compact morphologies and well as high stellar masses, which we discuss in further details in Section 5.

2.2 Gas-phase abundances in low-redshift galaxies

For comparison, we included a sample of local galaxies and nebulae with abundance measurements from [Izotov et al. \(2006\)](#), [Pilyugin et al. \(2012\)](#), [Berg et al. \(2016, 2019\)](#), [Annibali et al. \(2019\)](#), [Méndez-Delgado et al. \(2024\)](#), and [Grossi et al. \(2025\)](#) with $z \lesssim 0.1$. Specifically, the sample of metal-poor galaxies of [Izotov et al. \(2006\)](#) come from the Data Release 3 (DR3) of the Sloan Digital Sky Survey (SDSS, [York et al. 2000](#)). The abundances were derived through the so-called T_e method, where electron temperatures are estimated through flux ratios of optical auroral and strong lines of metals (e.g., $[\text{O III}]\lambda 4363/[\text{O III}]\lambda 5007$), and the majority of the sample have $12 + \log(\text{O/H}) \lesssim 8.5$. We took the abundances of O/H and N/O in the gas phase derived by [Izotov et al. \(2006\)](#) for these galaxies. There are 5 galaxies with $\log(\text{N/O}) > -0.5$, all of which, however, have signal-to-noise (S/N) in $[\text{O III}]\lambda 4363$ of $\text{S/N} \approx 1$ and thus do not have reliable temperature estimates. Therefore, we did not include these galaxies. We also used N/O and O/H derived by [Pilyugin et al. \(2012\)](#) for a sample of galaxies in the DR6 of SDSS using both the T_e method with auroral lines and the strong-line method. This sample covers $12 + \log(\text{O/H})$ above 8.5, although most of the galaxies still have lower metallicities. We further include N/O and O/H of 3

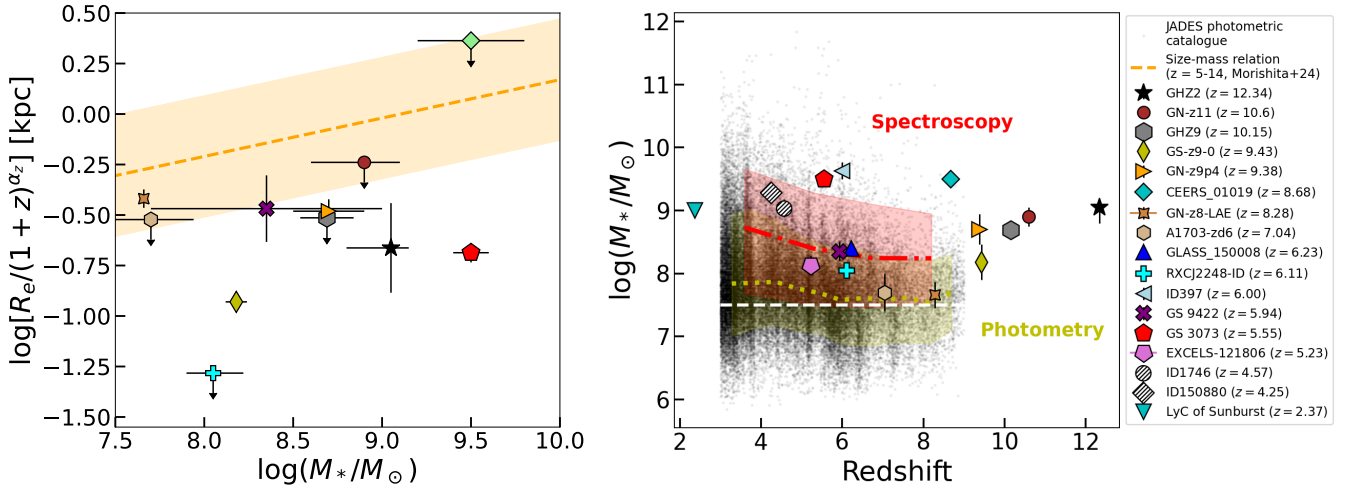


Figure 1. Global properties of high- z NOEGs in our sample. *Left*: size-stellar mass relation for NOEGs and a compilation of *JWST* galaxies at photometric redshift of $5 < z_{\text{photo}} < 14$ studied by Morishita et al. (2024). For the *JWST* sample, Morishita et al. (2024) fitted the redshift evolution of the relation with the parameter $\alpha_z = -0.44$, which we use to normalize R_e . We plot the best-fit linear model of Morishita et al. (2024) as the dashed orange line together with the 1σ dispersion in $\log R_e$ indicated by the shaded region. The NOEGs are generally more compact compared to galaxies at similar stellar masses. *Right*: stellar mass-redshift relation for NOEGs and JADES photometric sample at $3 < z_{\text{photo}} < 9$. The JADES sample has a 90% completeness at $M_* \gtrsim 10^{7.5} M_\odot$ as indicated by the dashed white line (see Simmonds et al. 2024). The dotted yellow line represents the median trend of the JADES photometric sample and the shaded region is bounded by the 10 percentile and 90 percentile lines. The dash-dotted red line represents the median trend of the JADES subsample with spectroscopic observations and the shaded region is bounded by the 10 percentile and 90 percentile lines. The NOEGs are relatively massive, and their selection is highly inhomogeneous and probably biased by their UV brightness, which allows for measurements of faint nitrogen lines.

extremely metal-poor H II regions with $12 + \log(\text{O/H}) \sim 7$ in the galaxy DDO 68 derived by Annibali et al. (2019), as well as 6 metal-poor dwarf galaxies with $12 + \log(\text{O/H}) \approx 7.4 - 7.9$ from Grossi et al. (2025). We also included a sample of dwarf galaxies from Berg et al. (2016, 2019) with abundances of O/H and C/O. Since the measurement of C/O usually relies on the UV carbon lines, there are not many determinations of the gas-phase C/O in local galaxies. Finally, the sample of Méndez-Delgado et al. (2024) includes 451 galaxies and H II regions with Galactic or extra-galactic origins, where the local galaxy sample of Izotov et al. (2006) is also included. From this sample, we took the measurements of O/H and Fe/O made by Méndez-Delgado et al. (2024) with corrections for temperature inhomogeneities. We note that whether or not to include the temperature corrections do not have any significant impact on our conclusions.

2.3 Stellar abundances in the Milky Way

We included a sample of MW stars observed by the SDSS Apache Point Observatory Galaxy Evolution Experiment (APOGEE) in the data release 17 (DR17, Abdurro'uf et al. 2022). APOGEE is a medium resolution¹ ($R \sim 22,500$), near infrared spectroscopic survey (15,140 - 16,940 Å) covering $\sim 650,000$ MW stars across both hemispheres. To derive chemical abundances for up to 20 different species, the APOGEE Stellar Parameter and Chemical Abundance Pipeline (ASPCAP, García Pérez et al. 2016) is used to fit individual absorption lines (either atomic or molecular) in the stellar spectra using the full-spectrum-fitting code, FERRE (Allende Prieto et al. 2006). Specifically, we used the allStarLite catalogue, applying the same quality cuts as in Belokurov & Kravtsov (2022) to exclude stars with problematic flags (e.g., STAR_BAD, LOW_SNR, PERSIST-related issues, EXTRATARG duplicates). We only consider red giant

stars, i.e. those with $1.5 < \log(g) < 3$ and $T_{\text{eff}} < 5300$ K excluding the most evolved red giant branch (RGB) stars as they show spurious N/O abundances. To be included in our sample, stars have to exhibit moderately small uncertainties (i.e., < 0.2 dex) in measurements of abundances of the following chemical elements: [Fe/H], [Mg/Fe], [C/Fe], [N/Fe], [O/Fe], [Si/Fe], [Al/Fe]. We also explicitly exclude stars that are part of the magcloud observing program. Distances are taken from the AstroNN catalogue (Mackereth & Bovy 2018; Leung & Bovy 2019), and proper motions from Gaia EDR3 (Gaia Collaboration et al. 2021a; Lindegren et al. 2021).

Where possible, we have compared chemical abundances in our APOGEE DR17 sample with those in GALAH DR4 (Buder et al. 2025) and have detected an unphysical trend in the behaviour of [O/Fe] as a function of [Fe/H] as reported by APOGEE DR17. We correct for this trend using median residuals between APOGEE DR17 and GALAH DR4 in bins of metallicity. The resulting corrected [O/Fe] values are validated using abundances of a sample of stars in the old and the intermediate-age disks of the Galaxy (sometimes referred to as the thick and the thin disks) published by Amarsi et al. (2019). Our corrected [O/Fe] abundances show a perfect agreement with those in the literature. Note that for this calibration procedure and for the analysis presented in this paper, we select old (thick) and intermediate-age (thin) disks using values of orbital eccentricity and z_{max} (amplitude of the vertical excursion about the Galactic plane) as published in the AstroNN catalogue.

To select GC stars from the clean APOGEE catalogue we cross-match with the GC membership catalogues of Vasiliev & Baumgardt (2021). Using Gaia EDR3 (Gaia Collaboration et al. 2021b) astrometry and photometry, Vasiliev & Baumgardt (2021) assign a membership probability between 0 and 1 for stars in the vicinity of 170 MW GCs. Adopting a membership probability of $> 50\%$ we recovered ~ 2500 stars across 27 clusters. Because we are interested in differentiating between generation one and two stars in GCs, we

¹ By the standard of the stellar community.

keep only the GCs with five or more member stars in our APOGEE catalogue.

Following the above initial cross-match, we then split members within each cluster into likely first- and second-generation stars. We used chemical abundance patterns to define the two generations, where the stars formed later are enhanced in N, Na, and Al but depleted in O and Mg compared to stars formed earlier (Bastian & Lardo 2018), and the demarcation is set at the average abundance pattern in each cluster. Starting with N and O, whose abundances are best measured in our sample, first-generation (1G) stars are defined as having $[N/O] \leq [O/Fe]_{\text{average}}$ and $[O/Fe] \geq [O/Fe]_{\text{average}}$. For the second-generation (2G) stars we apply the opposite cuts with the modification that $[O/Fe] \leq [O/Fe]_{\text{average}} - \sigma([O/Fe])$, where σ represents the standard deviation in $[O/Fe]$. This modification is necessary because the $[N/O]$ versus $[O/Fe]$ distribution in GCs is, in reality, a continuum, not two distinct populations and we would like to sample the endpoint of the distribution to capture the 2G stars (this is especially important in massive clusters like ω -Centauri which represents $\sim 30\%$ of our sample). We note that while the abundance distributions in GCs are usually continuous from the 1G to 2G stars, this does not necessarily imply continuous star formation in the past, but could be a result of bursts of star formation with stellar ejecta mixed with the ambient gas in different proportions (D’Ercole et al. 2008). The above definition with N/O automatically separates two generations in the N/O-O/H space. We also checked an alternative selection not involving N/O but leveraging the well-known Al-Mg anticorrelations among GC stars (e.g., Gratton et al. 2001). We did not use the Na-O anticorrelation due to the large uncertainties of Na in APOGEE (Jönsson et al. 2020) and the large spread in Na differences between APOGEE and GALAH (Buder et al. 2025). We selected 1G stars by requiring $[Al/Mg] \leq [Al/Mg]_{\text{average}} - 0.5\sigma([Al/Mg])$ and 2G stars by requiring $[Al/Mg] \geq [Al/Mg]_{\text{average}} + 0.5\sigma([Al/Mg])$. Our conclusions remain unchanged with the alternative selection. We used the cut involving N/O as our fiducial selection since 1) N measurements have lower uncertainties compared to Al measurements ($S/N(N)_{\text{median}} = 9 > S/N(Al)_{\text{median}} = 6$); 2) the Al-Mg cut is physically not independent of the N-O cut as the Mg-Al cycle occurs at higher temperatures compared to the CNO cycle.

Within our catalogue of GCs, we identified known nuclear star clusters (NSCs) following classifications by Pfeffer et al. (2021) and McKenzie et al. (2022). These include Omega Centauri (NGC 5139), NGC 6273, NGC 6656, and NGC 1851, which are thought to be the remnant nuclei of accreted dwarf galaxies. Among these, NGC 5139 alone contributes approximately 80% of the stars in the NSC subsample and around 40% of all stars in our combined GC/NSC sample. It is therefore essential to distinguish this cluster from the broader GC population. Beyond this numerical dominance, we also flag NSCs because they are believed to have hosted extended star formation episodes and to harbour more complex stellar populations than typical GCs (Neumayer et al. 2020). As a result, NSCs may exhibit distinct chemical abundance patterns, a point we return to in the analysis that follows.

3 DERIVATION OF PHYSICAL PROPERTIES OF NOEGS

In this section, we describe the derivation of physical properties, mainly the chemical abundances, for the compiled sample. The majority of the physical properties we used for our sample sources are directly from the literature listed in Tables 1 and 2. We refer readers to the original sources for details of the derivation and summarize several key points relevant to our analysis below.

Table 1. Global properties of a compilation of NOEGs from the literature at $0 \lesssim z \lesssim 12$ investigated in this work.

ID	Redshift	$\log M_{\star}/M_{\odot}$	R_e (pc)
Mrk 996 ^a	0.00544	8.7 ± 0.1	710 (220-430 [†])
Sunburst Arc (LyC) ^b	2.37	$9 (7^{\dagger})$	$31 (< 20^{\dagger})$
ID150880 ^c	4.25	$9.28^{+0.02}_{-0.04}$	-
UNCOVER-45924 ^d	4.46	-	$\lesssim 70$
ID1665 ^c	4.48	-	-
ID1746 ^c	4.57	9.03	-
ID1477 ^c	4.63	-	-
ID60001 ^e	4.69	$9.34^{+0.08}_{-0.10}$	600, 290
EXCELS-121806 ^f	5.23	$8.13^{+0.09}_{-0.06}$	-
GS_3073 ^g	5.55	9.5 ± 0.1	80-180
GS_9422 (tentative) ^h	5.94	7.7-9.0	90-200
ID397 ^c	6.00	9.63	-
RXJ2248-ID ⁱ	6.11	$8.05^{+0.17}_{-0.15}$	< 22
GLASS_150008 ^j	6.23	$8.4^{+0.4}_{-0.2}$	-
A1703-zd6 ^k	7.04	7.7 ± 0.24	< 120
GN-z8-LAE ^l	8.28	7.66 ± 0.02	143 ± 15
CEERS_01019 ^m	8.68	9.5 ± 0.3	790-910 [*]
GN-z9p ⁿ	9.38	8.7 ± 0.2	$118 \pm 16 (< 190)$
GS-z9 ^o	9.43	8.18 ± 0.06	110 ± 9
GHZ9 ^p	10.15	8.52-8.86	< 106
GN-z11 ^q	10.60	$8.9^{+0.2}_{-0.3}$	$196 \pm 12^*$
GHZ2 ^r	12.34	$9.05^{+0.10}_{-0.25}$	34-105

Notes.

References: ^a Berg et al. (2016); James et al. (2009); Thuan et al. (1996); ^b Vanzella et al. (2022); Sharon et al. (2022); Pascale et al. (2023); Welch et al. (2025); ^c Stiavelli et al. (2025); ^d Labb   et al. (2024); ^e Zhang et al. (2025); ^f Arellano-C  rdova et al. (2025); ^g Vanzella et al. (2010);   bler et al. (2023); Ji et al. (2024); ^h Cameron et al. (2024); Tacchella et al. (2025); ⁱ Topping et al. (2024); ^j Isobe et al. (2023); ^k Topping et al. (2025); ^l Navarro-Carrera et al. (2024); ^m Isobe et al. (2023); Larson et al. (2023); ⁿ Schaerer et al. (2024); ^o Curti et al. (2025); ^p Napolitano et al. (2025); ^q Cameron et al. (2023); Tacchella et al. (2023); Maiolino et al. (2024a);   lvez-M  rquez et al. (2025); ^r Castellano et al. (2024); Calab   et al. (2024).

[†] Values corresponding to a star cluster or an H II region/association rather than the whole galaxy.

^{*} With an additional point-source like component.

In Table 1, we summarize the global properties of our sample NOEGs including their redshift, stellar masses, and effective radii. The stellar mass is reported for the whole galaxy. For LyC of the Sunburst Arc, the stellar mass of this super star cluster alone is also reported. For the effective radius, it is measured in different photometric bands for different systems. For ID60001, the two effective radii correspond to two different components identified in F090W band of *JWST*/NIRCam by Zhang et al. (2025). For CEERS_01019 and GN-z11, there are both a point-source like component and an extended component and the effective radii correspond to the extended component. For Mrk 996, Thuan et al. (1996) measured a scale length of 0.42 kpc for the exponential disk component excluding the central starburst region, corresponding to an effective radius of 0.71 kpc for the disk. We also report the size of the central H II region in Mrk 996 according to James et al. (2009); for LyC, we report the upper limit on the size of the super star cluster described in Pascale et al. (2023).

In Table 2, we report the derived chemical abundances including O/H, N/O, C/O, Fe/O, and He/H. Not all sources have all these abundances measured or constrained due to the lack of required nebular emission lines in observations. We emphasize that, similar to the work by Schaerer et al. (2024), we do not attempt to re-derive abundances in published works. We discuss the validity of previous abundance derivations in Section 5. For some sources, emission

Table 2. Derived nebular properties for a compilation of NOEGs from the literature at $0 \lesssim z \lesssim 12$ investigated in this work.

ID	T_e (10^4 K)	n_e (cm^{-3})	$12 + \log(\text{O/H})$	$\log(\text{N/O})$	$\log(\text{C/O})$	$\log(\text{Fe/O})$	He/H
Mrk 996 (high density) ^a	1	10^7	$8.38^{+0.07}_{-0.08}$	-0.13 ± 0.28	-	-	0.072 ± 0.018
Mrk 996 (low density) ^a		170 ± 40	$8.36^{+0.17}_{-0.28}$	-1.43 ± 0.14	-0.22 ± 0.25	$-1.60^{+0.22}_{-0.33} \dagger$	0.091 ± 0.017
LyC (high density) ^b	-	10^5	8.03 ± 0.06	$-0.21^{+0.10}_{-0.11}$	-0.51 ± 0.05	-	-
LyC (low density) ^b		10^{3-4}	8.03 ± 0.06	-1.31 ± 0.12	-	-1.7 ± 0.2	0.08 ± 0.02
ID150880 ^c	1.49	203^{+500}_{-203}	$8.00^{+0.10}_{-0.08}$	$-0.88^{+0.15}_{-0.16}$	-	-	-
UNCOVER-45924 ^d	$2.6^{+0.5}_{-0.4} \dagger$	$10^{2-4} *$	$7.15 - 7.67 \dagger$	$0.20^{+0.06}_{-0.05} \dagger$	$-0.06^{+0.06}_{-0.05} \dagger$	-	-
ID1665 ^c	1.2	204^{+390}_{-204}	$8.26^{+0.15}_{-0.11}$	-0.93 ± 0.15	-	-	-
ID1746 ^c	1.59	790^{+2300}_{-590}	$7.92^{+0.13}_{-0.10}$	$-0.85^{+0.15}_{-0.14}$	-	-	-
ID1477 ^c	1.84	300*	$7.72^{+0.09}_{-0.07}$	$-0.62^{+0.11}_{-0.10}$	-	-	-
ID60001 ^c	1.61 ± 0.04	350 ± 180	7.75 ± 0.03	-0.76 ± 0.03	-	-	$0.12 \pm 0.02 \dagger$
EXCELS-121806 ^f	1.49 ± 0.11	870 ± 450	$7.97^{+0.05}_{-0.04}$	$-0.86^{+0.15}_{-0.11}$	-1.02 ± 0.22	-	-
GS_3073 (high density) ^g	1.45 ± 0.13	$5 \pm 1 \times 10^5$	$8.00^{+0.12}_{-0.09}$	$0.42^{+0.13}_{-0.10}$	$-0.38^{+0.13}_{-0.11}$	$> -1.84 - -1.24$	$0.07 \pm 0.01 \dagger$
		10^{2-4}	$8.00^{+0.12}_{-0.09}$	$-1.10^{+0.18}_{-0.20}$	-	$> -1.84 - -1.24$	$0.10 \pm 0.02 \dagger$
GS_9422 (tentative) ^h	1.83 ± 0.15	$\lesssim 10^3$	7.59 ± 0.01	< -0.85	-0.73 ± 0.03	$-1.03^{+0.15}_{-0.20}$	0.11 ± 0.01
ID397 ^c	1.43	300*	$7.96^{+0.10}_{-0.08}$	$-0.67^{+0.14}_{-0.13}$	-	-	-
RXJ2248-ID ⁱ	2.46 ± 0.26	$0.64 - 3.1 \times 10^5$	$7.43^{+0.17}_{-0.09}$	$-0.39^{+0.10}_{-0.08}$	$-0.83^{+0.11}_{-0.10}$	-	$0.166^{+0.018}_{-0.014}$
GLASS_150008 ^j	1.93 ± 0.12	$\lesssim 10^4$	$7.65^{+0.14}_{-0.08}$	$-0.40^{+0.05}_{-0.07}$	$-1.08^{+0.06}_{-0.14}$	-	0.142 ± 0.054
A1703-zd6 ^k	2.30 ± 0.32	$9.4 \pm 4.2 \times 10^4$	7.47 ± 0.19	-0.6 ± 0.3	-0.74 ± 0.18	-	$0.082 \pm 0.017 \dagger$
GN-z8-LAE ^l	1.73 ± 0.24	$\lesssim 10^4$	7.85 ± 0.17	-0.44 ± 0.36	-0.69 ± 0.21	-	-
CEERS_01019 (AGN) ^m	$1.5 \pm 0.5^*$	$1.1^{+3.3}_{-1.0} \times 10^3$	$8.37^{+0.13}_{-0.14}$	> -0.01	< -0.36	-	-
		$1.1^{+3.3}_{-1.0} \times 10^3$	$7.94^{+0.46}_{-0.31}$	> 0.28	< -1.04	-	-
GN-z9p4 ⁿ	2.30 ± 0.37	100*	7.38 ± 0.15	-0.59 ± 0.24	< -1.18	-	-
GS-z9-0 ^{o, s}	2.2 ± 0.2	650 ± 430	$7.49^{+0.11}_{-0.15}$	-0.93 ± 0.37	-0.90 ± 0.26	$-1.33^{+0.37}_{-0.85}$	-
GHZ9 ^p	-	100*	$6.69 - 7.69$	$-0.08 - 0.12$	$-0.96 - -0.45$	-	-
GN-z11 ^q	1.36 ± 0.13	100*	7.91 ± 0.07	> -0.25	> -0.78	$-0.86^{+0.22}_{-0.43}$	$0.073^{+0.046}_{-0.029} \dagger$
GHZ2 ^{r, s}	$2.12^{+0.27}_{-0.24}$	10^{3-5}	$7.44^{+0.26}_{-0.24}$	-0.25 ± 0.05	-0.74 ± 0.20	$-1.50^{+0.83}_{-1.00}$	-

Notes.

References: ^a Berg et al. (2016); James et al. (2009); Marques-Chaves et al. (2024); ^b Vanzella et al. (2022); Pascale et al. (2023); Welch et al. (2025); ^c Stiavelli et al. (2025); ^d Labb   et al. (2024); ^e Zhang et al. (2025); ^f Arellano-C  rdova et al. (2025); ^g   bler et al. (2023); Ji et al. (2024); ^h Cameron et al. (2024); Tacchella et al. (2025); ⁱ Topping et al. (2024); ^j Isobe et al. (2023); ^k Topping et al. (2025); ^l Navarro-Carrera et al. (2024); ^m Isobe et al. (2023); Larson et al. (2023); ⁿ Schaerer et al. (2024); ^o Curti et al. (2025); ^p Napolitano et al. (2025); ^q Cameron et al. (2023); Tacchella et al. (2023); Maiolino et al. (2024a);   lvarez-M  rquez et al. (2025); Ji et al. (2025b); Nakane et al. (2024); ^r Castellano et al. (2024); Calab   et al. (2024); Zavala et al. (2024, 2025); ^s Nakane et al. (2025).

[†] These values are newly derived in this work based on the reported fluxes in the literature. See Section 3 for details.

* These are assumed values as no observational constraints from narrow emission lines are available.

All temperatures listed are for the high-ionization zone traced by O^{2+} .

line fluxes required for abundance derivations were measured but the abundances were not reported in the corresponding works. We supplement derivations of these chemical abundances previously not reported for the following sources, Mrk 996, UNCOVER-45924, ID60001, GS_3073, A1703-zd6, and GN-z11. In what follows, we give a brief overview of the previous and new abundance derivations. We further discuss details of specific abundance measurements in Sections 4 and 5.

First of all, for 19 out of 22 sources in our sample NOEGs, the oxygen abundances are constrained by the so-called direct method, where the electron temperature, T_e , is derived using the flux ratio of $[\text{O III}]\lambda 4363/[\text{O III}]\lambda 5007$ or $[\text{O III}]\lambda 1666/[\text{O III}]\lambda 5007$. For LyC, while Pascale et al. (2023) applied photoionization models instead of the direct T_e method to fit all abundances, they included measured fluxes of $[\text{O III}]\lambda 1666$ and $[\text{O III}]\lambda 5007$. Thus, we consider that the temperature is also well constrained in this case. For CEERS_01019, Isobe et al. (2023) assumed a typical temperature of $(1.5 \pm 0.5) \times 10^4$ K as no observational constraint is available. For GHZ9, Napolitano et al. (2025) estimated O/H indirectly based on the equivalent width of $[\text{C III}]\lambda\lambda 1906, 1908$ as well as the strong emission line ratio of $[\text{Ne III}]\lambda 3869/[\text{O II}]\lambda\lambda 3726, 3729$, obtaining a range of 1 dex in O/H. In principle, since Napolitano et al. (2025) measured the fluxes of $[\text{O III}]\lambda 1666$ and $[\text{O III}]\lambda 4363$, the electron temperature can be es-

timated assuming no significant density variation is present (e.g., presence of a broad-line region). However, since GHZ9 is an X-ray detected AGN, it is unclear whether the $[\text{O III}]\lambda 1666$ has contamination from the broad-line region (BLR). Thus, we adopt the conservative range of metallicity estimated by Napolitano et al. (2025). We note that for GN-z11 and GHZ2, although $[\text{O III}]\lambda 5007$ is redshifted out of the wavelength range of NIRSpec, this line is detected in the follow-up MIRI observations and is combined with $[\text{O III}]\lambda 4363$ or $[\text{O III}]\lambda 1666$ to provide temperature estimates (Alvarez-M  rquez et al. 2025; Calab   et al. 2024). With the derived temperatures, abundance ratios of N/O, C/O, Fe/O, and He/H are subsequently derived using flux ratios of relevant strong emission lines from the rest-frame UV to the optical and the calculated emissivities.

Next, we comment on the abundance derivations for specific sources. For Mrk 996, LyC, and GS_3073, we report two abundance patterns for each source, since at least two nebular components with different gas densities have been found in observations (James et al. 2009; Pascale et al. 2023;   bler et al. 2023; Ji et al. 2024). Notably, the derived N/O is always higher for the high-density component compared to the low-density component in these sources. The existence of high-density regions is also reported for RXJ2248-ID, A1703-zd6, and GN-z11 (Topping et al. 2024, 2025; Maiolino et al. 2024a). For GN-z11, there is a component with a extremely high den-

sity reaching $n_e \sim 10^{10} \text{ cm}^{-3}$ and potentially tracking the BLR of an AGN (Maiolino et al. 2024a; Maiolino et al. in prep.). The fiducial abundances reported by Cameron et al. (2023) and Álvarez-Márquez et al. (2025) were derived by assuming observed metal lines come from a low-density region with $n_e = 100 \text{ cm}^{-3}$. Regardless, the contribution from a high density region would likely only strengthen the upper limit on the derived N/O based on UV emission lines (see e.g., Ji et al. 2024). The density effect is further discussed in Section 5.

For Mrk 996, James et al. (2009) did not calculate the abundance of Fe, although $[\text{Fe III}]\lambda 4658$ is significantly detected in the VLT/VIMOS spectrum. Following the approach adopted by Thuan et al. (1995) and Izotov et al. (2006), we calculated $\text{Fe}^{2+}/\text{H}^+$ using

$$12 + \log\left(\frac{\text{Fe}^{2+}}{\text{H}^+}\right) = \log\left(\frac{[\text{Fe III}]\lambda 4658}{\text{H}\beta}\right) + 6.498 + \frac{1.298}{t} - 0.498 \log(t), \quad (1)$$

where $t \equiv T_e/10^4 \text{ K}$ and we assumed $t \approx 1$ to be consistent with the analysis of James et al. (2009). We obtained $12 + \log(\text{Fe}^{2+}/\text{H}^+) = 6.31 \pm 0.02$. The ionization correction factor (ICF) for Fe^{2+} to account for ionization species not observed is given by

$$\text{ICF}(\text{Fe}^{2+}) = -1.377v + 1.606 + 1.045/v, \quad (2)$$

where $v \equiv \text{O}^+/\text{(O}^+ + \text{O}^{2+}\text{)}$. The above equation is applicable when $12 + \log(\text{O/H}) > 8.2$, which is the case for Mrk 996 based on the measurements of James et al. (2009). According to James et al. (2009), $v = 0.54 \pm 0.19$, and thus $\text{ICF}(\text{Fe}^{2+}) = 2.8_{-0.8}^{+1.3}$. As a result, $12 + \log(\text{Fe/H}) = 6.76_{-0.14}^{+0.17}$ and $\log(\text{Fe/O}) = -1.60_{-0.33}^{+0.22}$. We note that this calculation only applies to the low-density component identified by James et al. (2009), as $[\text{Fe III}]\lambda 4658$ is only observed in this component in Mrk 996.

For UNCOVER-45924, Labb   et al. (2024) provide flux measurements for emission lines from the JWST micro shutter assembly (MSA, Ferruit et al. 2022) PRISM spectrum (with a nominal spectral resolution of $R \sim 100$) but do not derive the chemical abundances. We derived the abundances of O, N, C, and He using fluxes reported in Tables 2, 4, and 5 of Labb   et al. (2024). For the oxygen abundance, we first estimated the electron temperature for the high-ionization zone from $[\text{O III}]\lambda 4363/[\text{O III}]\lambda 5007$. We used the PYTHON package PyNEB (Luridiana et al. 2015) with the atomic database of CHIANTI (v10, Dere et al. 1997; Del Zanna et al. 2021) and Tayal & Zatsarinny (2017). We also corrected the line ratio using the Balmer decrement assuming an average SMC bar extinction curve of Gordon et al. (2003) and an intrinsic $\text{H}\alpha/\text{H}\beta$ of 3.1 typical for the narrow-line region (NLR) of AGN (Osterbrock & Ferland 2006). At the low density limit of $[\text{O III}]\lambda 5007 (n_e < 10^4 \text{ cm}^{-3})$, we derived $T_e(\text{O}^{2+}) = 2.6_{-0.4}^{+0.5} \times 10^4 \text{ K}$. Using $[\text{O III}]\lambda 5007/\text{H}\beta$, we obtained $12 + \log(\text{O}^{2+}/\text{H}^+) = 7.07 \pm 0.20$. For the temperature of the low ionization zone, we used $[\text{O II}]\lambda\lambda 3726, 3729/[\text{O II}]\lambda\lambda 7320, 7331$ also measured by Labb   et al. (2024) and corrected for dust attenuation. However, we found $T_e(\text{O}^+) > 3 \times 10^4 \text{ K}$, even higher than $T_e(\text{O}^{2+})$, which is not expected for NLRs of AGN (Dors et al. 2020). A potential explanation is the low-density approximation no longer holds in this case, as $[\text{O II}]\lambda\lambda 3726, 3729/[\text{O II}]\lambda\lambda 7320, 7331$ is more sensitive to the density variation compared to $[\text{O III}]\lambda 4363/[\text{O III}]\lambda 5007$ due to the low critical density of $[\text{O II}]\lambda\lambda 3726, 3729 (\sim 10^4 \text{ cm}^{-3})$. This would result in overestimation of $T_e(\text{O}^+)$. Unfortunately, no density constraints are available for the NLR of UNCOVER-45924. If we considered the low density limit and kept $T_e(\text{O}^+) > 3 \times 10^4 \text{ K}$, O^+ would be negligible compared to O^{2+} . The ICF for $\text{O}^{2+} + \text{O}^+$ is usually derived from $\frac{\text{He}^{2+} + \text{He}^+}{\text{He}^+}$ (Torres-Peimbert & Peimbert 1977). However, Labb   et al. (2024) argue the measured fluxes of He I and

He II lines are dominated by the BLR. As an alternative solution, we took an average ICF(O) of 1.2 from a sample of AGN NLRs analyzed by Dors et al. (2020), yielding $12 + \log(\text{O/H}) = 7.15 \pm 0.20$. If we assumed $n_e = 10^4 \text{ cm}^{-3}$, $T_e(\text{O}^{2+})$ remains largely unchanged but $T_e(\text{O}^+) = 1.14 \pm 0.04 \times 10^4 \text{ K}$, leading to $12 + \log(\text{O/H}) = 7.67 \pm 0.10$. We list both values in Table 2 and consider the range as a systematic uncertainty.

We also derived N/O and C/O for UNCOVER-45924. In the rest-frame optical, $[\text{N II}]\lambda 6583$ is significantly blended with $\text{H}\alpha$ in the PRISM spectrum and is a subdominant component within the blended line. Thus, we did not use the $[\text{N II}]$ flux fitted by Labb   et al. (2024). Instead, we used the UV lines of $[\text{N III}]\lambda\lambda 1746-1754$ and $[\text{O III}]\lambda\lambda 1661, 1666$. While these lines can have both narrow and broad components and they cannot be separated in the PRISM spectrum, Labb   et al. (2024) argue all UV lines are broad based on their spectral energy distribution (SED) fitting. If we follow the interpretation of Labb   et al. (2024), the derivation of N/O would be subject to the complex physical conditions in the BLR (e.g., Temple et al. 2021). Due to the similar ionization potentials and critical densities, $[\text{N III}]/[\text{O III}]$ is a good tracer of N/O when the ionization condition and density are not extreme. At densities of $n_e \lesssim 10^9 \text{ cm}^{-3}$, the emissivity ratio of $[\text{N III}]/[\text{O III}]$ is insensitive to density. At $n_e > 10^9 \text{ cm}^{-3}$, the emissivity ratio of $[\text{N III}]/[\text{O III}]$ starts to drop with increasing density until $n_e \sim 10^{11} \text{ cm}^{-3}$. Therefore, deriving N/O from $[\text{N III}]/[\text{O III}]$ at $n_e < 10^9 \text{ cm}^{-3}$ gives a *lower limit* (see, e.g., photoionization models of Ji et al. 2024). Another difficulty is the temperature of the gas. To solve these problems, we compared the measured $[\text{N III}]/[\text{O III}]$ with a set of CLOUDY (c17.03, Ferland et al. 2017) photonionization models similar to those computed by Ji et al. (2024), with $n_{\text{H}} = 10^9 \text{ cm}^{-3}$ and a range of ionization parameters (U)², O/H, and N/O. Details of the models can be found in Appendix A. We fixed $12 + \log(\text{O/H}) = 7.41$, the average of the two values listed in Table 2. Thus, the only free parameters are U and N/O, which are jointly constrained by $[\text{N IV}]\lambda 1486/[\text{N III}]\lambda\lambda 1746-1754$ and $[\text{N III}]\lambda\lambda 1746-1754/[\text{O III}]\lambda\lambda 1661, 1666$. We show the comparison between observed ratios and model predictions in Appendix A. The best-fit value we obtained is $\log(\text{N/O}) = 0.20_{-0.05}^{+0.06}$. Similarly, we derived the relative abundance of carbon for UNCOVER-45924 by using the flux ratio of $[\text{C III}]\lambda\lambda 1906, 1908/[\text{O III}]\lambda\lambda 1661, 1666$. To constrain the ionization parameter, we tried both $[\text{N IV}]\lambda 1486/[\text{N III}]\lambda\lambda 1746-1754$ and $[\text{C IV}]\lambda\lambda 1548, 1551/[\text{C III}]\lambda\lambda 1906, 1908$. The ionization parameter constrained by $[\text{C IV}]\lambda\lambda 1548, 1551/[\text{C III}]\lambda\lambda 1906, 1908$ is roughly 0.5 dex lower than that constrained by $[\text{N IV}]\lambda 1486/[\text{N III}]\lambda\lambda 1746-1754$ (see Appendix A). This could be due to either a highly stratified ionization structure (i.e., N IV) probes a more highly ionized region compared to C IV) or resonant scattering of C IV, 1548, 1551. Regardless, the two ionization parameters would only result in 0.1 dex difference in the derived C/O, with the lower-ionization case we obtained from C IV/C III predicting a lower C/O.

Finally, for ID60001, GS_3073, A1703-zd6, and GN-z11, there are significant detections of $\text{He I}\lambda 5876$ and $\text{He I}\lambda 3889$ in their corresponding JWST/NIRSpec spectra (  bler et al. 2023; Ji et al. 2024, 2025b; Bunker et al. 2023; Maiolino et al. 2024a; Zhang et al. 2025), but no derivation of He/H has been carried out thus far. Among all optical transitions of He I, $\text{He I}\lambda 5876$ is usually the strongest one and is relatively insensitive to density variations and radiative transfer effects (e.g., Benjamin et al. 2002; Olive & Skillman 2004; Aver et al. 2015). This makes $\text{He I}\lambda 5876$ a good tracer of He^+/H^+

² The ionization parameter is defined as the ratio between the ionizing flux and the product of the hydrogen density and the speed of light.

once combined with a close-by hydrogen recombination line such as $H\beta^3$. For ID60001, we use the measured ratio of $He\,\lambda 5876/H\beta$ and $He\,\lambda 4686/H\beta$ to calculate He^+/H^+ and He^{2+}/H^+ using PyNEB. We assumed $T_e = (1.61 \pm 0.04) \times 10^4$ K and $n_e = 345^{+184}_{-172} \text{ cm}^{-3}$ as derived by [Zhang et al. \(2025\)](#). While the T_e was derived for O^{2+} , which lies in an ionization zone in between He^+ and He^{2+} , the contribution from He^{2+}/H^+ to the He/H is very small ($\sim 2\%$ of He^+/H^+) and $T_e(He^+)/T_e(O^{2+})$ is usually close to 1 (in this case ~ 0.99 based on the average relation computed with photoionization models for $H\,\text{II}$ regions by [Izotov et al. 2013](#)). Since He^0 might also coexist with H^+ , one also needs to estimate He^0/H^+ . However, the abundance ratio of $He^0/(He^+ + He^{2+})$ is usually less than 2% especially for ionized gas with high ionization parameters ([Izotov et al. 2014](#)). Therefore, we assume the contribution from He^0 is negligible. The above analysis leads to a final helium abundance of $He/H = 0.12 \pm 0.02$, higher than the solar reference of 0.084 but with a relatively large uncertainty. Such an enhancement of helium has also been found in a few other NOEGs as derived by [Yanagisawa et al. \(2024\)](#), although density variation could in principle bias the result, which we further discuss in Section 4.4. Similarly, we derived He/H for A1703-zd6 using the measurements of $He\,\lambda 5876/H\beta$, $T_e(O^{2+})$, and n_e reported by [Topping et al. \(2025\)](#).

For GS_3073, we used the narrow component of $He\,\lambda 5876$, $He\,\lambda 4686$, and $H\beta$ measured from the NIRSpec/IFU high-resolution grating spectrum by [Übler et al. \(2023\)](#) and used $T_e = (1.45 \pm 0.13) \times 10^4$ K derived by [Ji et al. \(2024\)](#). Since all lines involved are permitted, we used both densities from the high-density component and low-density component in GS_3073 to obtain a range of He/H , which is $He/H \sim 0.07 - 0.10$. For GN-z11, we used $He\,\lambda 3889$, $He\,\lambda 1640$, and $H\delta$ and used $T_e = (1.36 \pm 0.13) \times 10^4$ K ([Álvarez-Márquez et al. 2025; Ji et al. 2025b](#)). We assumed $n_e = 100 \text{ cm}^{-3}$ and obtained $He/H = 0.073^{+0.046}_{-0.029}$. Raising the density to $n_e = 1000 \text{ cm}^{-3}$ would lower He/H by 0.003. One caveat of this approach is the radiative transfer of $He\,\lambda 3889$. This is because the lower level of $He\,\lambda 3889$ is the ground level of the triplet state, which is metastable. As a result, even low-density gas can become optically thick to $He\,\lambda 3889$. The value of He/H we derived for GN-z11 at the optically thin limit can thus be considered as a lower limit.

4 COMPARISONS OF CHEMICAL ABUNDANCE PATTERNS

In this section, we compare chemical abundance patterns of NOEGs to those of local stars and galaxies. It is worth noting that the chemical abundances for galaxies including NOEGs are gas-phase abundances traced by emission lines from ionized gas. In contrast, the chemical abundances of local stars are obtained through observations of absorption lines in the stellar atmosphere (see Section 2.3). We emphasize that we make no assertion on what population of stars is illuminating the gas in the NOEGs (as possible proto-GCs). Rather, we are inspecting whether the chemical composition of stars in the MW GCs matches that in the ISM of the NOEGs – linking the chemical composition of stellar atmospheres to the gas-phase abundances measured in our sample of high- z galaxies. Since carbon, oxygen,

³ Here we do not consider stellar absorptions underlying these lines (e.g., [Olive & Skillman 2004; Hsyu et al. 2020; Yanagisawa et al. 2024](#)), which should be modest for the high- z SF galaxies and have a much smaller impact compared to measurement uncertainties and systematic uncertainties we discussed.

and iron are observed to be depleted onto dust grains in the ISM (see e.g., [Jenkins 2009](#)), one expects the gas-phase abundances of these metals to differ from the abundances in stars born later from the same ISM by certain depletion factors ([Gunasekera et al. 2023](#)). Among the elements we investigated, nitrogen and helium do not deplete. For oxygen and carbon, the relative depletions are likely modest, with a typical value of 0.1–0.2 dex in the MW ([Jenkins 2009](#), although carbon depletion has a large uncertainty). The element that is most affected by dust depletion is Fe, where the depletion is usually larger than 1 dex along MW sightlines ([Jenkins 2009](#), and references therein). We discuss this effect in more detail in Section 4.3.

4.1 Nitrogen and oxygen abundance

We start by inspecting the abundance patterns of nitrogen and oxygen. While oxygen is mainly enriched by massive stars ($M_\star > 8 M_\odot$), there are different proposed channels for nitrogen enrichment. At low metallicities [$12 + \log(O/H) < 8$], nitrogen can be enriched either by massive stars, leading to a nearly constant N/O with small scatters (e.g., [Matteucci 1986](#)), or by intermediate-mass fast-rotating stars ($4 M_\odot < M_\star < 7 M_\odot$) through rotational mixing and released by stellar winds, which would lead to a relatively large scatter in N/O ([Henry et al. 2000; Meynet & Maeder 2002; Kobayashi et al. 2020](#)). At high metallicities [$12 + \log(O/H) > 8.2$], the enrichment of nitrogen in galaxies is mainly ascribed to winds from AGB stars with $2 M_\odot < M_\star < 8 M_\odot$ and is typically delayed by $\sim 0.1 - 1$ Gyr compared to the enrichment of oxygen for the global chemical evolution of galaxies (e.g., [Henry et al. 2000](#)). The above physical picture fits a plateau of subsolar N/O at low O/H and a nearly linear scaling between N/O and O/H at high O/H in observations of local galaxies, although the transitional O/H likely depends on the star formation efficiency (SFE, [Vincenzo et al. 2016](#)). While the above picture applies to the chemical evolution of the whole galaxies, the chemical imprints in star clusters can be drastically different with enhanced N from massive AGB stars with a delay time as short as 40 Myr.

In Figure 2 we compare N/O and O/H between NOEGs (large colored symbols), MW stars (density contours), and local metal-poor galaxies (small open circles). Additionally, we distinguish MW stars currently in the field – most of which originated in the disk (blue and green contours) – from those observed in surviving Galactic globular clusters (orange and red contours). When interpreting these distributions, it is important to consider the different selection biases that affect the reported chemical measurements. In particular, the metallicity distributions (traced by O/H) for ionized gas in local SF galaxies and stars in the MW are shaped by distinct observational and physical factors. Two main challenges complicate the detection and chemical characterization of local low-metallicity galaxies. First, such systems are intrinsically rare at $z \sim 0$ ([Izotov et al. 2006; Pilyugin et al. 2012](#)). Second, they are also faint, as lower-mass galaxies tend to be less chemically evolved (i.e., the mass-metallicity relation, [Tremonti et al. 2004; Andrews & Martini 2013](#)). Together, these effects lead to an under-representation of both low and high O/H values in the metallicity distribution of the local metal-poor galaxy sample (small open circles). These can be compared to stars in the Galactic disk, which trace a different environment: the MW – a more massive (~ 2 orders of magnitude higher than the metal-poor galaxies) and chemically evolved system, comparable in stellar mass to an L_* galaxy. As shown in Figure 2, most MW stars occupy the high-O/H region of the diagram. In contrast, the metallicity distributions of Galactic GCs in panels b) and c) reflect the varying star formation histories of their progenitor systems, such as accreted dwarf galaxies

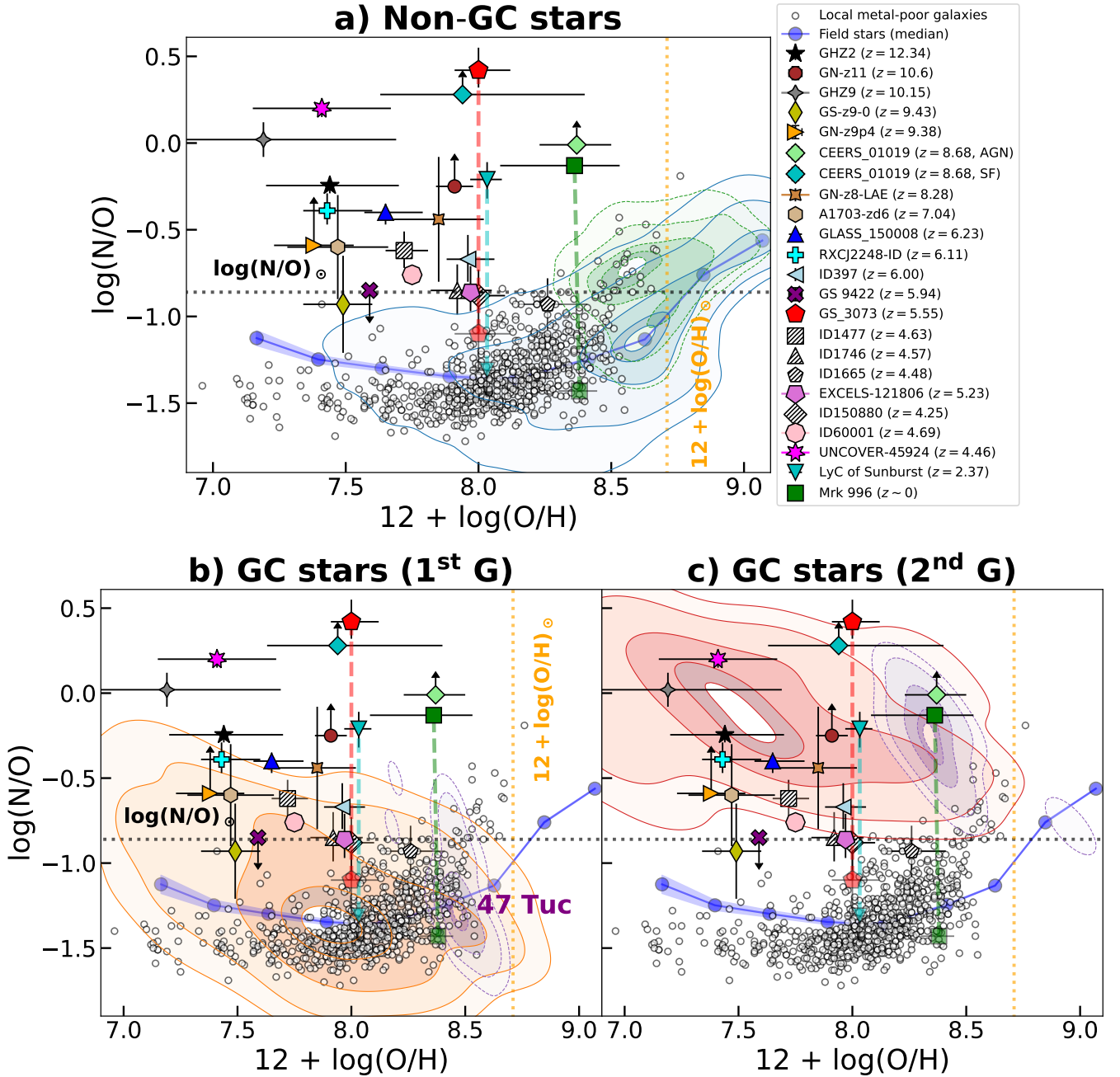


Figure 2. Distributions of NOEGs in the N/O versus O/H space in comparison with local galaxies and stars. Derived abundances for NOEGs come from Castellano et al. (2024); Cameron et al. (2023, 2024); Curti et al. (2025); Schaerer et al. (2024); Isobe et al. (2023); Larson et al. (2023); Topping et al. (2024, 2025); Ji et al. (2024); Übler et al. (2023); Pascale et al. (2023); James et al. (2009); Arellano-Córdova et al. (2025); Napolitano et al. (2025); Navarro-Carrera et al. (2024); Stiavelli et al. (2025); Zhang et al. (2025) and also this work. Systems showing two abundances connected by dashed lines have their higher abundances derived for high-density components ($n_e \gtrsim 10^5 \text{ cm}^{-3}$) decomposed from the observed spectra, and their lower abundances derived for low-density components ($n_e < 10^4 \text{ cm}^{-3}$). Derived abundances for local galaxies come from Izotov et al. (2006); Pilyugin et al. (2012); Annibali et al. (2019); Grossi et al. (2025). The contours correspond to probability distributions of abundances of MW stars compiled from Abdurro'uf et al. (2022) computed by the kernel density estimation function KDEPLOT from the PYTHON package SEABORN. Five contour levels are plotted corresponding to 5, 16, 50, 84, and 95 percentiles of the distributions, respectively. *Top:* abundance patterns of non-GC stars in the MW, where stars with $\log g < 1.5$, $\log g > 3$, or $T_{\text{eff}} > 5300 \text{ K}$ are excluded. Stars with azimuthal velocities of $v_t \geq 150 \text{ km s}^{-1}$ trace the thin disk and have an overall higher N/O, which are plotted as green contours with dashed boundaries. The cyan shaded region represents the median trend of MW field stars with no error cut in abundances (selected with $1.5 < \log g < 3$, $T_{\text{eff}} < 5300 \text{ K}$, and $v_t < 150 \text{ km s}^{-1}$) with 1σ median uncertainties. *Bottom:* abundance patterns of GC stars (excluding NSC stars) in the MW divided into 1st and 2nd generations. The abundance patterns of stars in the GC 47 Tuc are plotted as purple contours with dashed boundaries. Overall, the abundances of NOEGs are more consistent with those of GC stars, among which the 2nd-generation GC stars better overlap with NOEGs at $\log(N/O) > -0.5$.

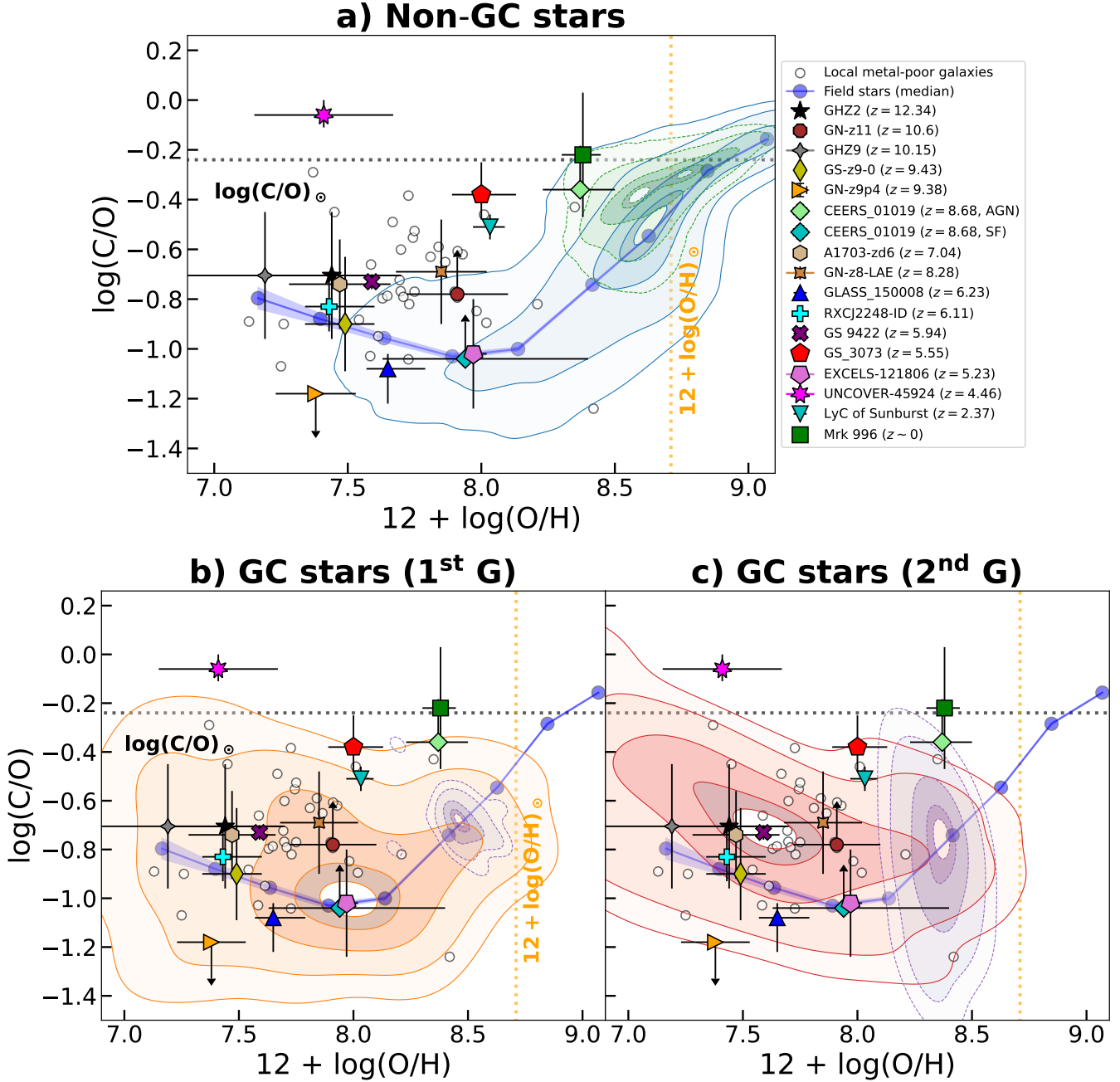


Figure 3. Distributions of NOEGs in the C/O versus O/H space in comparison with local galaxies and stars. Derived abundances for NOEGs come from Castellano et al. (2024); Cameron et al. (2023, 2024); Curti et al. (2025); Schaerer et al. (2024); Isobe et al. (2023); Larson et al. (2023); Topping et al. (2024, 2025); Ji et al. (2024); Übler et al. (2023); Pascale et al. (2023); Marques-Chaves et al. (2024); Arellano-Córdova et al. (2025); Navarro-Carrera et al. (2024); Napolitano et al. (2025) and also this work. Derived abundances for local galaxies come from Berg et al. (2016, 2019). The contours correspond to probability distributions of abundances of MW stars compiled from Abdurro'uf et al. (2022) computed by the kernel density estimation function `KDEPLOT` from the `PYTHON` package `SEABORN`. Five contour levels are plotted corresponding to 5, 16, 50, 84, and 95 percentiles of the distributions, respectively. *Top:* abundance patterns of non-GC stars in the MW, where stars lying on the thin disk and stars with $\log g < 1.5$, $\log g > 3$, or $T_{\text{eff}} > 5300$ K are excluded. Stars with azimuthal velocities of $v_t \geq 150$ km s⁻¹ trace the thin disk and have an overall higher C/O, which are plotted as green contours with dashed boundaries. The cyan shaded region represents the median trend of MW field stars with 1σ median uncertainties. *Bottom:* abundance patterns of GC stars (excluding NSC stars) in the MW divided into 1st and 2nd generations. While NOEGs appear to overlap with the low-metallicity tail of the non-GC stars, they better overlap with GC stars.

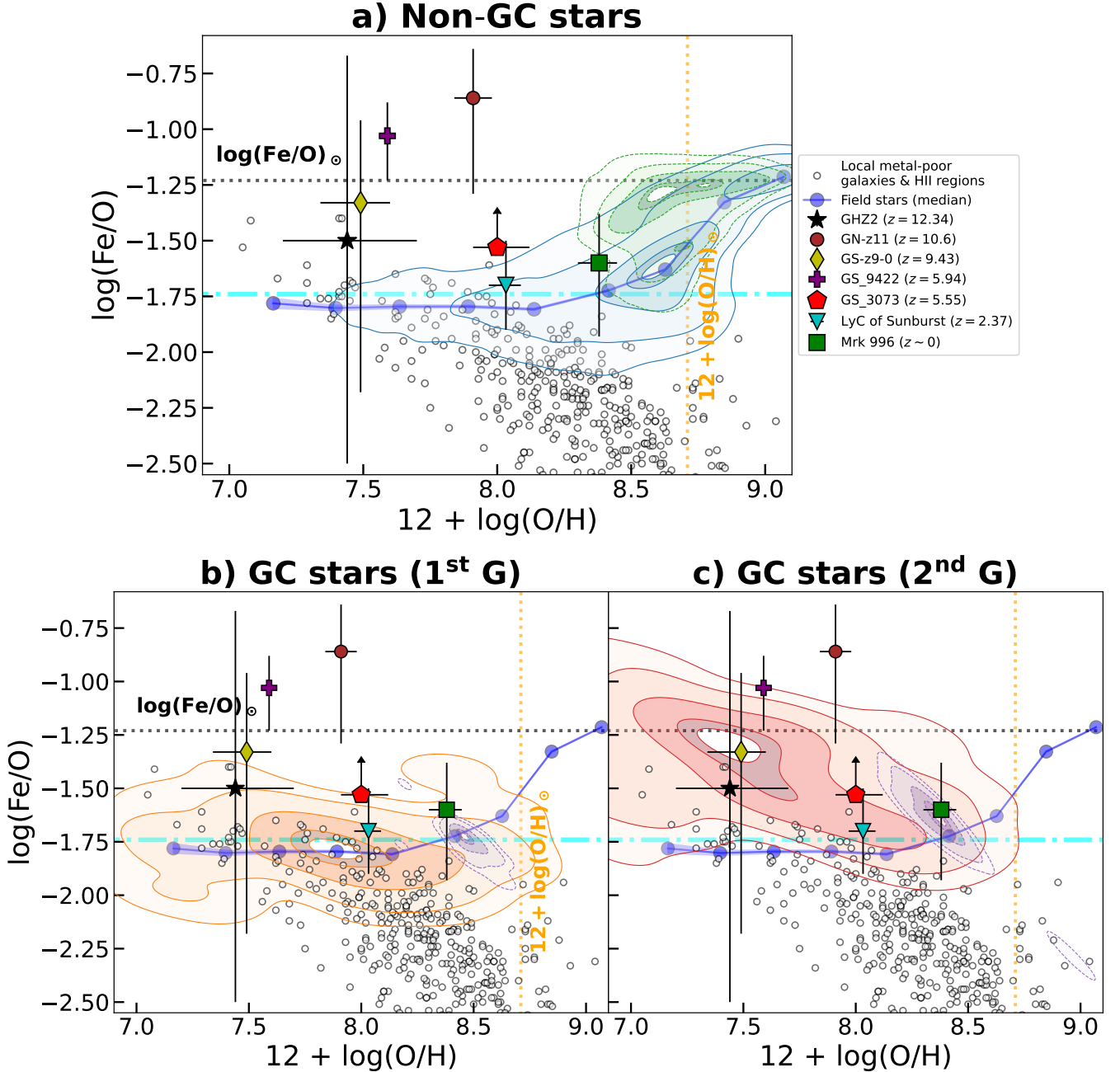


Figure 4. Distributions of NOEGs in the Fe/O versus O/H space in comparison with local galaxies and stars. Derived abundances for NOEGs come from Cameron et al. (2023, 2024); Nakane et al. (2024, 2025); Ji et al. (2025b, 2024); Übler et al. (2023); Welch et al. (2025) and also this work. Derived abundances for local galaxies and H II regions from Méndez-Delgado et al. (2024) are plotted as open circles, which reach $\log(\text{Fe/O}) \sim -3$ outside the range shown in the current figure. The horizontal dash-dotted cyan line is the asymptotic line of Fe/O for local galaxies and H II regions derived by Méndez-Delgado et al. (2024). The contours correspond to probability distributions of abundances of GC stars compiled from Abdurro'uf et al. (2022) computed by the kernel density estimation function `KDEPLOT` from the `PYTHON` package `SEABORN`. Five contour levels are plotted corresponding to 5, 16, 50, 84, and 95 percentiles of the distributions, respectively. *Top:* abundance patterns of non-GC stars in the MW, where stars lying on the thin disk and stars with $\log g < 1.5$, $\log g > 3$, or $T_{\text{eff}} > 5300$ K are excluded. Stars with azimuthal velocities of $v_t \geq 150 \text{ km s}^{-1}$ trace the thin disk and have an overall higher Fe/O, which are plotted as green contours with dashed boundaries. The cyan shaded region represents the median trend of MW field stars with 1σ median uncertainties. *Bottom:* abundance patterns of GC stars (excluding NSC stars) in the MW divided into 1st and 2nd generations. While some NOEGs appear to overlap with the low-metallicity tail of the non-GC stars, they also overlap with GC stars.

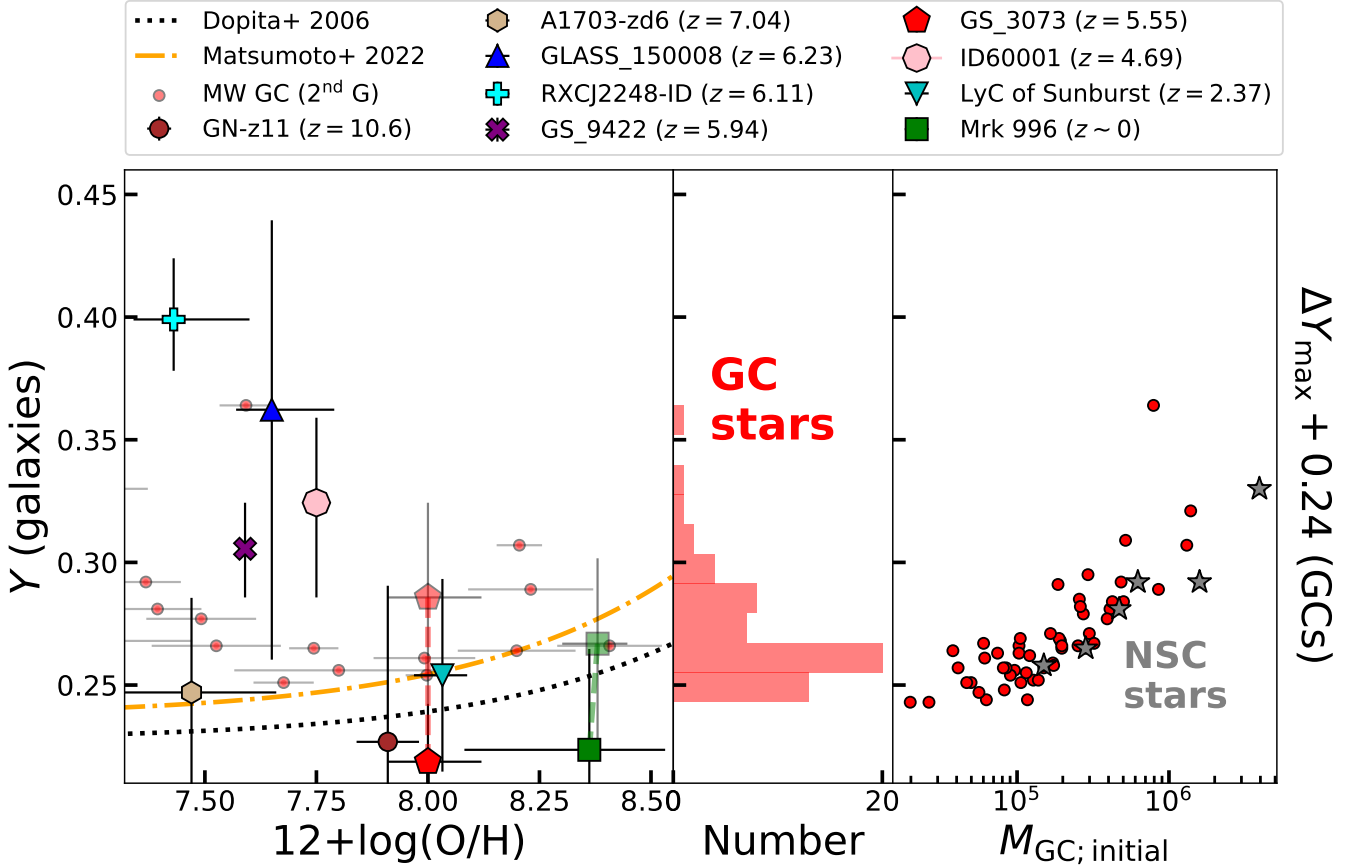


Figure 5. *Left:* Distributions of NOEGs in the Y (i.e., mass fraction of He) versus O/H space in comparison with local galaxies and stars. Derived abundances for the LyC of the Sunburst Arc come from [Welch et al. \(2025\)](#). Derived abundances for GS_9422, RXCJ2248-ID, and GLASS_150008 come from [Yanagisawa et al. \(2024\)](#). For GN-z11, A1703-zd6, GS_3073, ID60001, and Mrk 996, we derived their He abundances based on the measurements of He I and He II emission lines. In comparison, we also plot 1) Y as a function of O/H for local galaxies fitted by [Dopita et al. \(2006\)](#) and [Matsumoto et al. \(2022\)](#), and 2) maximum Y enhancement in individual MW GCs as a function of O/H averaged over the 2G stars. *Middle:* distributions of Y for a sample of local GC stars measured by [Milone et al. \(2018\)](#). *Right:* maximum enhancement in Y (see text) for a sample of local GC stars versus the inferred initial masses of the GCs measured by [Milone et al. \(2018\)](#), where accreted NSCs of previous dwarf galaxies are marked as star symbols. The NOEGs show a tentative trend of decreasing Y with increasing metallicity, which might be connected to the masses of clusters formed in these systems or caused by the bias in deriving Y (see text for details).

and the early MW. Since the contribution of globular clusters to overall star formation declines sharply with increasing metallicity (see [Belokurov & Kravtsov 2023](#)), their stars exhibit lower average O/H than both local galaxies and MW field stars.

Local SF galaxies from SDSS form a relatively tight sequence with roughly constant N/O of $\log(N/O) \approx -1.5$ for low-metallicity systems with $12 + \log(O/H) < 8.0$. At high metallicities, N/O of local galaxies scales nearly linearly with O/H. Similar scaling relations between N/O and O/H have also been found in spatially resolved regions of galaxies on scales of ~ 1 kpc ([Belfiore et al. 2017; Schaefer et al. 2020](#)). Meanwhile, it is clear from the top panel of Figure 2 that stars in the MW exhibit a similar scaling relation, despite that the majority of the stars are more metal-rich compared to SDSS galaxies and thus trace mainly the secondary nitrogen source. At lower metallicities, field halo stars with $12 + \log(O/H) < 7.7$ show slightly elevated N/O ratios, with the largest deviations near $12 + \log(O/H) \approx 7$. Several factors likely contribute to this trend in the Milky Way halo. First, below $12 + \log(O/H) < 7.7$, stars from the so-called *Aurora* population, which formed during the early, pre-disk phase of MW evolution, begin to appear ([Belokurov & Kravtsov 2022; Kane et al.](#)

[2025](#)

. Up to $\sim 50\%$ of Aurora's star formation may have occurred in massive clusters, potentially boosting its overall N/O ratios ([Belokurov & Kravtsov 2023](#)). Second, a selection bias affects nitrogen measurements at low metallicity. As nitrogen features weaken with declining abundance and opacity, detecting them requires high S/N spectra. To mitigate the S/N effect on the median trend (mainly at low O/H) of MW field stars, we did not apply any cut in the measurement uncertainties of relevant elements when plotting. Finally, APOGEE reports nitrogen abundances under 1D LTE assumptions. These are likely overestimated at low metallicities due to uncorrected 3D non-LTE effects (see e.g., [Lind & Amarsi 2024](#)). Note that despite these biases, it should still be possible to carry out a relative comparison of the abundances of the MW field and the GC stars.

It is worth noting that different populations of the MW disk stars have distinct abundance offsets. To illustrate this, we made a rough cut based on the azimuthal velocity (in galacto-centric cylindrical polar coordinates), v_t , where we assumed stars with $v_t \geq 150 \text{ km s}^{-1}$ come from the so-called "thin" disk and stars with $v_t < 150 \text{ km s}^{-1}$ come from the so-called "thick" disk. While the thin/thick disk distinction is a clear oversimplification of the MW's complex chromo-chemo-

dynamical structure, we use it here as a rough proxy to separate metal-rich stars formed at different epochs and in different Galactic environments. Stars in the thin disk (dashed green contours) exhibit higher N/O at fixed O/H than those in the thick disk (solid contours). This is consistent with the general view that the thin disk is significantly younger, having formed in the outer Galaxy from lower-density gas and with lower star formation efficiency. Since the gas-phase metallicity, as quantified by oxygen, is an α element, the higher N/O abundances in the thin disc also reflect a lower overall α abundance compared to the thick disk (hence, the “ α -poor disc”; [Minchev et al. 2013](#); [Haywood et al. 2013](#); [Rix & Bovy 2013](#); [Bensby et al. 2014](#); [Hayden et al. 2015](#); [Magrini et al. 2018](#)).

Compared to local galaxies and MW disk stars, NOEGs, by their definition, have significantly higher N/O at the same (gas-phase) O/H. Such a difference is particularly apparent at $12 + \log(\text{O/H}) < 8.0$, where N/O in local galaxies and MW disk stars roughly forms a plateau. The stars in MW GCs, on the other hand, clearly exhibit nitrogen enhancement compared to SDSS galaxies and MW disk stars. In the bottom panel of Figure 2, one can see that while the 1G GC stars have an overall similar distribution in terms of N/O and O/H compared to the MW field stars, the 2G GC stars show nearly ubiquitous enhancement of nitrogen with $(\text{N/O}) \gtrsim (\text{N/O})_0$. The 2G GC stars also show overall lower O/H compared to the 1G GC stars. These lower oxygen levels in the 2G stars become readily apparent when oxygen and iron levels are compared as we show later. The offset in O/H within GCs is associated with the so-called Na-O anti-correlation, where the abundance of Na increases as the abundance of O decreases. The standard explanation involves depletion of O due to the CNO cycle and the production of Na from the NeNa cycle in stellar nucleosynthesis at high temperatures. In observations, the Na-O anticorrelation has also been observed in main-sequence turn-off stars and sub-giants in GCs ([Gratton et al. 2001](#)), which rules out the possibility that this anticorrelation is driven by internal nucleosynthesis in stars at later times as the required temperature ($T > 3 \times 10^7$ K) is much higher than what is expected for these stars. Therefore, the lower oxygen abundances seen in the 2G GC stars is a reflection of the abundances of the ISM they formed in, which has been enriched in Na via the NeNa cycle and depleted in O via the CNO cycle which operated in the hot 1G stars.

The oxygen-poor NOEGs ($12 + \log(\text{O/H}) < 8.0$) appear to trace the transition from the 1G GC stars to the 2G GC stars with the decreasing oxygen abundance. In particular, three of the metal-poor yet nitrogen-rich NOEGs, GHZ2 ($z = 12.34$, black star) GHZ9 ($z = 10.15$, gray four-pointed star) and UNCOVER-45924 ($z = 4.46$, magenta seven-pointed star) overlap with the dense part of the distribution of the 2G GC stars. Still, we caution that both GHZ9 and UNCOVER-45924 host AGN and lack high-resolution spectra for key emission lines, and thus their oxygen abundances have large uncertainties. For NOEGs, the sequence of increasing N/O at decreasing O/H is also noted, for example, by [Zhang et al. \(2025\)](#). This trend appears not exact if we include more metal-rich sources at $12 + \log(\text{O/H}) \geq 8.0$, especially CEERS_01019 at $z = 8.68$, GS_3073 at $z = 5.55$, LyC of the Sunburst Arc at $z = 2.37$, and Mrk 996 at $z \sim 0$. Their abundances might better match those of metal-enriched GCs. Indeed, if we focus on a single metal-enriched GC, 47 Tuc (which is the most massive MW in-situ GC), the 2G GC stars roughly reproduce the N/O and O/H of these NOEGs. Thus, it is possible that the N/O-O/H anticorrelation also exists in more metal-rich NOEGs, but the sequence for these NOEGs starts at higher O/H. It should be noted that among these NOEGs, there are three systems showing two abundance patterns, which are GS_3073 at $z = 5.55$, the LyC of the Sunburst Arc at $z = 2.37$, and Mrk 996 at

$z \sim 0$. As described in Section 3, the two abundance patterns are derived by separating emission-line spectra into high- and low-density (pressure) components. The high-density regions consistently show elevated N/O, while the low-density components exhibit N/O ratios aligned with the local galaxy sequence. This suggests the presence of chemical stratification, where regions near super star clusters or nuclear star clusters are more nitrogen-enriched ([James et al. 2009](#); [Pascale et al. 2023](#); [Ji et al. 2024](#)). This also implies that the observed nitrogen enhancement in early galaxies may be confined to compact, high-gas-density regions associated with intense star formation, such as stellar clusters.

Given the above results, one question is whether there is any observational bias driving the distribution of NOEGs in the N/O-O/H space. The selection of the current NOEGs is from surveys/programs with different selection functions and is clearly not homogeneous, and NOEGs are mostly UV-bright galaxies with relatively high stellar masses as shown in Figure 1. The intrinsic brightness of NOEGs probably facilitates the measurements of nebular lines but also biases their selection. For the metal-enriched NOEGs with $12 + \log(\text{O/H}) \geq 8.0$, for example, they might not reflect the true distribution of NOEGs due to the following reasons. The LyC of the Sunburst Arc is identified because the galaxy is strongly lensed. The galaxy, GS_3073, hosts an unobscured AGN, which might boost the luminosities of its emission lines. The local BCD, Mrk 996, only exhibits nitrogen enhancement when there is enough spectral resolution to separate the different density components. Another general question is whether the nitrogen enhancement is ubiquitous at high redshift, or if we are simply biased by the bright NOEGs. While this is not the main focus of this work, recent studies using stacks of high- z galaxies suggest an overall enhancement in N/O at $z > 4$ despite potentially large scatter in individual sources ([Hayes et al. 2025](#); [Isobe et al. 2025b](#)). The general enhancement of N/O would be expected if galaxies underwent cluster-dominated star formation at early times, which we further discuss in Section 5.

4.2 Carbon abundance

Similar to nitrogen, the enrichment of carbon has a significant contribution from the secondary process and is delayed with respect to that of oxygen ([Garnett et al. 1995](#); [Nicholls et al. 2017](#); [Kobayashi et al. 2020](#)). This leads to a primary+secondary C/O versus O/H relation similar to the N/O versus O/H relation. As shown in the top panel of Figure 3, the field stars in the MW do show a fast increase in C/O at high O/H with a turnover metallicity of $12 + \log(\text{O/H}) \approx 8.0$. At $12 + \log(\text{O/H}) \lesssim 7.5$, there is again a increase in C/O of field stars. This likely reflects a combination of our signal-to-noise selection bias and the use of 1D LTE models in APOGEE abundance determinations (see above). We therefore refrain from assigning a physical interpretation to this low-metallicity upturn.

Compared to stellar determinations of C/O, since the nebular determinations of C/O usually rely on the coverage of the strong UV carbon doublet, $\text{C III} \lambda\lambda 1906, 1908$, or the detection of faint recombination lines of carbon, there are not many measurements in the gas phase for local galaxies. Most of the NOEGs show sub-solar C/O consistent with the low-O/H tail of the MW disk stars. One exception is the nitrogen-loud AGN host galaxy, UNCOVER-45924 at $z = 4.46$, which shows a super-solar C/O at sub-solar O/H. While the enhancement of C/O to super-solar values is also reported for a galaxy at $z = 12.5$, this occurs at $12 + \log(\text{O/H}) < 7$ and is potentially explained by the yield from (low-energy) supernovae of the Population III stars ([D'Eugenio et al. 2024](#)). For local galaxies, there is also a large spread in C/O at low O/H, which could be a

combined effect of large uncertainties propagated from the UV-line measurements and the intrinsic spread in C/O caused by the bursty star-formation history in dwarf galaxies (Berg et al. 2016, 2019).

As shown in the bottom panels of Figure 3, the distribution of the 1G GC stars closely matches the distribution of low-O/H field stars, while the distribution of the 2G GC stars exhibits slightly enhanced average C/O (traced by the contour center) with lowered O/H. However, compared to the field sample, the GC stars also show a wider spread in C/O, which, combined with the generally lower O/H, makes GC stars better match the abundances of NOEGs. For the relatively metal-enriched NOEGs at $12 + \log(\text{O/H}) \geq 8.0$, they still show sub-solar to solar C/O and could be compatible with the abundance pattern of the 2G stars of the massive GC 47 Tuc. Still, the abundances of the most metal-rich NOEGs in our sample, Mrk 996 and possibly CEERS_01019 (if its lines are mostly contributed by AGN-ionized regions; Isobe et al. 2023), also overlap with the contours of MW disk stars. For UNCOVER-45924, its possibly super-solar C/O is not seen in typical GC stars. However, as we show later in Section 5, such an enhancement in C/O is observed in a particular NSC, NGC 5139. The overall sub-solar C/O of NOEGs indicates the prevalence of significantly super-solar N/C in these systems. The anomalous N/C of NOEGs is also recognized in previous studies (e.g., Isobe et al. 2023, 2025b; Ji et al. 2024; Schaefer et al. 2024; Topping et al. 2024). At the equilibrium of the CNO cycle, it is expected that N/C would be significantly enhanced (~ 2 dex above solar, Maeder et al. 2015). However, the N/C ratio from, for example, the yields of AGB stars, can vary in a wide range from sub-solar to super-solar depending on the degree of the CNO processing, which is very different in different sets of models (e.g., Herwig 2004; Karakas & Lattanzio 2007; Ventura et al. 2013), as it depends on the efficiency of convection in the stellar envelope and on the number of the third dredge-up episodes, strongly affected by the mass loss rate adopted, although models with low mass loss rates overpredict the C+N+O abundances in 2G stars. Alternatively, yields of WR stars, TDEs, and SMSs can potentially explain the elevated N/C (Isobe et al. 2023; Watanabe et al. 2024).

In summary, in the C/O versus O/H plane, the low-metallicity MW field stars, GC stars, and NOEGs occupy broadly overlapping regions. While C/O alone does not single out a unique counterpart to NOEGs, the fact that 2G GC stars and NOEGs remain consistent in C/O provides a valuable sanity check. This reinforces the stronger connection already evident from their matching N/O ratios.

4.3 Iron abundance

As another important tracer of chemical evolution, iron is produced early by CCSNe and later by Type Ia supernovae (SNe) in large amounts. The enrichment channel through Type Ia SNe makes Fe abundance sensitive to a timescale of ~ 1 Gyr after the initial burst of star formation (Maoz & Mannucci 2012). Thus, one expects Fe to trace a longer timescale of chemical evolution compared to N.

As shown in the top panel of Figure 4, the non-GC stars in the MW show a strong increase in Fe/O close to solar O/H (known as the low “ α -knee” if one replaces the x axis with Fe/H and revert the y axis, Wallerstein 1962; Tinsley 1979), consistent with the delay enrichment of Fe. Also, the thin disk is more oxygen-poor (or α -poor) compared to the thick disk. In comparison, local galaxies and H II regions with gas-phase Fe/O measurements by Méndez-Delgado et al. (2024) show a small overlap with the MW non-GC stars roughly at $7.5 < 12 + \log(\text{O/H}) < 8.0$, with a tentative low-O/H tail of enhanced Fe/O. Méndez-Delgado et al. (2024) argue that there is actually a low-metallicity plateau at $\log(\text{Fe/O}) \approx -1.74$ indicated

by the dash-dotted line in Figure 4, which is also consistent with the Fe/O plateau seen in the MW field stars. As O/H increases, the gas-phase Fe/O of local galaxies and H II regions show a systematic decrease in contrast to the increasing trend in MW field stars. The interpretation by Izotov et al. (2006) and Méndez-Delgado et al. (2024) for this anticorrelation between Fe/O and O/H in the gas phase is the increased depletion of Fe onto dust grains at high metallicities. From the observational studies along the MW sightlines, it has been shown that there is significant variation of Fe depletion (by 1 – 2.5 dex, Jenkins 2009), although there lack clear evidence of how the amount of depletion correlates with the metallicity. Besides the dust depletion, another caveat is that the derivation of the gas-phase Fe abundance mostly relies on a single Fe species, Fe^{2+} . At low metallicities, Fe^{2+} is not the dominant Fe species, and thus the accuracy of the Fe abundance is subject to the accuracy of the ICF (see e.g., the discussions by Rodríguez & Rubin 2005; Kojima et al. 2021; Méndez-Delgado et al. 2024). Alternatively, pair-instability supernovae (PISNe) or hypernovae (HNe) from VMSs might produce Fe enhancement at low O/H (e.g., Kojima et al. 2021; Isobe et al. 2022; Watanabe et al. 2024).

Regarding NOEGs, measurements of the Fe abundance become much more difficult, although not impossible. For the high- z NOEGs we considered, only four of them have estimations of Fe/O, yet all with large uncertainties. While the Fe abundance of the Sunburst Arc is derived from the optical Fe line, $[\text{Fe III}]\lambda 4658$ (Welch et al. 2025), all other sources have different ways of estimating their Fe abundances. For GS_3073 at $z = 5.55$, Ji et al. (2024) use high-ionization Fe lines including $[\text{Fe IV}]\lambda\lambda 2829, 2835$ and $[\text{Fe VII}]\lambda 6087$ to estimate the Fe abundance. However, these Fe lines are blended with Mg II and $[\text{Ca V}]$, respectively, in the low-resolution NIRSpec PRISM spectrum, and thus Ji et al. (2024) can only make a rough estimation assuming a range of contamination. The lower limit in Fe/O for GS_3073 makes it compatible with the local galaxies and H II regions. For GS_9422 at $z = 5.94$, Tacchella et al. (2025) use the detection of another high-ionization Fe line, $[\text{Fe V}]\lambda 4227$, in the NIRSpec PRISM spectrum (and potentially in the medium-resolution NIRSpec G395M spectrum). Notably, GS_9422 has a gas-phase Fe/O compatible or higher than the solar value, tracing the low-metallicity tail of the distribution of local galaxies studied by Izotov et al. (2006). Finally, for GS-z9-0 at $z = 9.43$, GN-z11 at $z = 10.6$, and GHZ2 at $z = 12.34$, the Fe abundances reported by Nakane et al. (2024, 2025) are the *stellar* abundances and rely on continuum fitting of the rest-frame UV spectra obtained with *JWST*/NIRSpec medium-resolution ($R \sim 1000$) and low-resolution ($R \sim 100$) spectra. This approach assumes the whole UV continuum is dominated by young stellar populations, whereas the AGN-like UV lines and extremely high densities ($n > 10^9 \text{ cm}^{-3}$, i.e. BLR-like) indicate the presence of an AGN in GN-z11 (Maiolino et al. 2024a). Regardless, as shown by Ji et al. (2025b) and Nakane et al. (2024, 2025), the continuum excess observed in the UV spectrum of GN-z11 would also imply an enhanced *nebular* Fe abundance if one interprets the UV continuum as being dominated by an AGN accretion disk.

If we adopt the measurement of Nakane et al. (2024) and consider the Fe/O as the stellar abundance, GN-z11 would have a super-solar Fe/O only ~ 430 Myr after the Big Bang. In fact, both GS_9422 and GN-z11 would not have sufficient time for the enrichment by the main population of the Type Ia SNe. Thus, one needs to invoke either small range enrichment (e.g., within a single proto star cluster) by a few early Type Ia SNe (for a delay time as short as 30 Myr, see Greggio & Renzini 1983), or enrichment by PISNe or HNe (Nakane et al. 2025). Either of the enrichment scenarios would imply the Fe enhancement occurred as early as the N enhancement. Interestingly,

as recently shown by Isobe et al. (2025a) through stacking of JADES galaxies at $4 < z < 7$, supersolar Fe/O is also found at low O/H for galaxies with high specific star-formation rates and blue UV slopes. The measured Fe/O, however, cannot be simultaneously reproduced with the measured Si/O based on some models of CCSNe, PISNe, HNe, or CCSNe with the mixing-and-fallback process + Type Ia SNe inspected by Isobe et al. (2025a).

From the bottom panels of Figure 4, the MW GC stars show a plateau in Fe/O closely matching that of field stars in the 1G population and enhanced Fe/O at lowered O/H in the 2G population. This behavior can be interpreted again as the 1G stars are born in a similar chemical environment as metal-poor field stars and yet the 2G stars are affected by the depletion of oxygen by the CNO cycle through the enrichment of the 1G stars. While the Fe/O-O/H distributions of the 2G GC stars are again more consistent with that of NOEGs, due to the uncertain Fe abundance measurements in NOEGs, we cannot draw a strong conclusion.

4.4 Helium abundance

Last but not least, we examine the abundance of helium. Unlike metals, helium is abundant and has a large contribution from Big Bang Nucleosynthesis (BBN). The BBN leads to a primordial mass fraction of $Y_p \approx 0.24 - 0.25$, and stellar nucleosynthesis and subsequent CCSNe enrichment lead to a slight increase in Y in the ISM as a function of metallicity. The abundance of helium is also connected to the abundance anomalies seen in GCs. In GCs, significant spread in He abundances among stars are observed, with the 2G stars usually having higher Y compared to the 1G stars (e.g., Milone et al. 2018). While the average helium enhancement between the two generations is modest ($\Delta Y \sim 0.01$), the *maximum* helium variation in GCs can reach $\Delta Y \gtrsim 0.05$, which depends on the initial mass and the luminosity of the GC (Milone et al. 2018). The enhancement of helium is mainly via hydrogen burning in the core of hot stars in the first generation. Therefore, the maximum helium variation is in principle an indicator of how complex the actual stellar populations in GCs are. For example, the cluster displaying the largest He-variation reported in Milone et al. (2018), is NGC 2808. NGC 2808 is among the most massive MW GCs (Baumgardt & Hilker 2018), demonstrating the connection between cluster mass and He-enhancement. The final helium spread in observations can be explained as a combined effect of stellar-wind enrichment and accretion of pristine gas, and can potentially reflect the formation timescale of GCs (i.e., higher ΔY for GCs forming with a longer time and/or with a shorter enrichment timescale, Gieles et al. 2025).

In galaxies, the nebular abundance of helium can be derived from optical transitions of He I and He II, with He⁺ usually being the dominant species. Recently, Yanagisawa et al. (2024) investigated helium abundances of three *JWST*-selected NOEGs, which are GS_9422 at $z = 5.94$, RXCJ2248-ID at $z = 6.11$, and GLASS_150008 at $z = 6.23$, and they reported a tentative positive correlation between N/O and Y . Yanagisawa et al. (2024) argued that CCSNe cannot explain the helium enhancement they found, and the helium enhancement must be related to the CNO cycle. In the left panel of Figure 5, we plot Y versus metallicity for 8 NOEGs in comparison with the observed relations in the local Universe inferred by Dopita et al. (2006) and Matsumoto et al. (2022). Our comparison to local Y -O/H relations is a consistency check only – even if N/O-enhanced phases exhibit localized N enrichment and possibly small ΔY , these episodes are not expected to shift the low- z , galaxy-integrated Y -O/H locus. There appears to be an anticorrelation between Y and O/H, but no clear monotonic Y -N/O trend. This is because the more oxy-

gen enriched NOEGs including GN-z11, GS_3073, Sunburst Arc, and Mrk 996 are actually more nitrogen enhanced compared to the extremely helium enhanced NOEG, RXCJ2248-ID. In addition, we caution that the NOEG, A1703-zd6, although has low O/H, does not show any significant enhancement in Y . Thus, with the current data, it is unclear whether there is any true underlying Y -O/H relation

A related question is whether there is any measurement bias or physical mechanism to enhance the apparent helium abundance. From the perspective of measurement systematics, as already pointed out by Yanagisawa et al. (2024), Y would be overestimated if the helium-line emitting gas has very high electron densities. Indeed, as shown by James et al. (2009); Pascale et al. (2023); Ji et al. (2024); Isobe et al. (2025b), density enhancement (and variation) might be ubiquitous in NOEGs, and would be reasonable if their spectra are dominated by dense proto-GCs. Specifically, for RXJ2248-ID, Topping et al. (2024) report electron densities up to 10^5 cm^{-3} as probed by UV lines, whereas Yanagisawa et al. (2024) assumed the low-density limit in their fiducial modeling. With PyNEB and the CHIANTI atomic data set (and assuming the optically thin case or He I $\lambda 5876$), we found the emissivity of He I $\lambda 5876$ at $T_e = 1.5 \times 10^4 \text{ K}$ is a factor of 1.7 higher at $n_e = 10^5 \text{ cm}^{-3}$ compared to the low-density case of $n_e = 10^2 \text{ cm}^{-3}$. This means at $n_e = 10^5 \text{ cm}^{-3}$ and an intrinsic $Y = 0.25$, the apparent helium mass fraction is $Y \approx 0.36$ if one assumes $n_e = 10^2 \text{ cm}^{-3}$. Thus, it is plausible that there is no extreme helium enhancement in NOEGs if helium lines are predominantly produced in dense clouds. This might also explain the seemingly low Y in the most N/O-enhanced object, GS_3073. If the Y enhancement in other NOEGs at low O/H is biased by underestimated gas densities, given the generally large measurement uncertainties in Y , and the potential intrinsic scatter due to different gas dilution, retrieving the intrinsic Y -O/H or Y -N/O trend in NOEGs would require more statistics.

Alternatively, if the observed helium lines in NOEGs are from low-density gas, the enhancement seems only significant at low metallicities in some NOEGs. In the left panel of Figure 5, we plot individual MW GCs (small red dots) to compare with NOEGs, where we use the maximum helium variations in GCs from Milone et al. (2018) plus the primordial mass fraction of 0.24 to represent the maximum helium enhancement seen in individual GCs. The O/H of GCs is averaged over their 2G stars since the helium enhancement is present in the 2G. The enhanced helium abundances are seen both at $12 + \log(\text{O/H}) < 8$ and $12 + \log(\text{O/H}) > 8$, with the extremely helium enhanced GC, NGC 2808, reaching the location of GLASS_150008 ($z = 6.23$). In the middle panel of Figure 5, we show the number distribution of the maximum helium spread in MW GCs from Milone et al. (2018), which clusters at a low value of $\Delta Y = 0.1$. In the right panel of Figure 5, we further plot the maximum helium spread as a function of the initial mass of the GC, showing that the extreme enhancement of $\Delta Y > 0.5$ is only found at massive clusters of $M_{\text{GC, initial}} > 10^6 M_{\odot}$. As a result, one potential explanation for the enhanced Y in some metal-poor NOEGs is the more efficient formation of massive GCs. In observations of MW GCs, however, there is no clear hint of any initial mass-metallicity relation (e.g., in the sample we used and presented by Milone et al. 2018). We do note that the recovery of the initial mass of GCs might be uncertain as they lost 50 - 80% of their initial masses, and the mass distributions of GCs we observed today might be biased to high-mass GCs that have lost less of their masses (e.g., Kruijssen 2015; Reina-Campos et al. 2018; Baumgardt et al. 2019).

Another possibility is that the enhanced Y is connected to NSCs, which reserve most of their initial masses due to the deep gravitational potentials and on-average exhibit more enhanced Y as shown

in the right panel of Figure 5, possibly due to their extended star formation histories. The occurrence of NSCs in local early-type galaxies appears to depend on the *current - day* stellar mass of the host galaxies, with an occurrence rate peaking at $M_\star \approx 10^9 M_\odot$ and dropping at both lower and higher masses (Neumayer et al. 2020). From Table 1, the more metal-rich NOEGs already have $M_\star > 10^{8.5} M_\odot$ or even $M_\star \gtrsim 10^9 M_\odot$ if we exclude the local Mrk 996, meaning they will evolve into $M_\star > 10^9 M_\odot$ galaxies observed today. In such a scenario, it is plausible that the NSC growth in the more massive and metal-rich NOEGs is less efficient as those in lower mass NOEGs that eventually quenched as lower-mass early-type galaxies. As a second explanation, the reduced Y enhancement at high-mass and metal-rich NOEGs might imply less cluster-dominated star formation. However, this scenario seems incompatible with the even stronger nitrogen enhancement in metal-rich NOEGs.

To summarize, in our NOEG sample, there is no clear indication of a correlation between Y and N/O, although there might be enhanced Y in some low-O/H NOEGs. Underestimated electron densities could potentially lead to the rise of Y at low O/H. Regardless, if the helium enhancement is real, its presence might be connected to the efficiency of forming massive GCs or NSCs in these galaxies.

5 DISCUSSION

In this section, we discuss our results from two perspectives. On one hand, we discuss the systematic uncertainties involved in current abundance measurements and how they might impact our interpretations. On the other hand, we discuss the physical interpretations based on the similar abundance patterns of NOEGs and GC stars.

5.1 Validity of the abundance measurements at high redshift

Measurements of gas-phase chemical abundances usually involve a number of assumptions. Even when the electron temperature is constrained by auroral-to-strong line ratios such as $[\text{O III}]\lambda 4363/[\text{O III}]\lambda 5007$, as is the case for most of the NOEGs we investigated, bias can still arise due to inhomogeneous ISM conditions, such as density or temperature variations (e.g., Peimbert 1967; Peimbert et al. 2017; Méndez-Delgado et al. 2023).

As we mentioned in the last section, density variation exists in at least three NOEGs, with the high-density regions having $n_e \sim 10^{5-7} \text{ cm}^{-3}$ and the low-density regions having $n_e \lesssim 10^4 \text{ cm}^{-3}$. The density inhomogeneity would bias the abundance derivation if the electron density reaches the critical densities of emission lines involved in the abundance derivation. However, since the rest-frame UV emission lines involved generally have high critical densities (e.g., $n_{\text{critical}} > 10^9 \text{ cm}^{-3}$ for $\text{N III}]\lambda 1750, \text{N IV}]\lambda 1486, \text{O III}]\lambda\lambda 1661, 1666, \text{C III}]\lambda 1908, \text{C IV}]\lambda\lambda 1548, 1551$), N/O derived from UV line ratios are relatively insensitive to density enhancement (Ji et al. 2024; Isobe et al. 2025b; Martinez et al. 2025). An interesting question is whether “normal” N/O can be probed with UV lines. There might be two limiting factors for achieving this. First, due to the enhanced line emissivity in dense gas, the observed UV lines from galaxies might preferentially sample N/O in dense gas environments (e.g., star clusters). Second, given the sensitivity of most *JWST* observations, for galaxies with no intrinsic N/O enhancement, it would be challenging to verify purely based on the upper limits of UV lines (Isobe et al. 2025b; Zhu et al. 2025).

In the optical, $[\text{N II}]\lambda 6583$ is the only relatively strong nitrogen transition typically used for deriving the nitrogen abundance and has a critical density of $n_{\text{critical}} \sim 10^5 \text{ cm}^{-3}$. This means

that a bias would arise if $n_e > 10^4 \text{ cm}^{-3}$, especially when using $[\text{N II}]\lambda 6583/[\text{O II}]\lambda\lambda 3726, 3729$ to infer N⁺/O⁺ in typical practices ($n_{\text{critical}, [\text{O II}]\lambda 3727} \sim 10^4 \text{ cm}^{-3}$). Among the 22 NOEGs we compiled, 14 have their N/O derived from UV semi-forbidden transitions and thus the inferred abundance ratios are insensitive to density enhancement. For GS_3073, due to the presence of broad emission lines in the rest-frame optical, the semi-forbidden transitions in the rest-frame UV might also have a broad component (which remains unresolved in the low-resolution NIRSpec/PRISM spectrum). However, as shown by Ji et al. (2024), the existence of any UV broad component would only imply a stronger intrinsic nitrogen enhancement. The UV region of UNCOVER-45924 also suffers from contamination by broad lines, and we have discussed this issue in Section 3, where we can still estimate N/O (or its lower limit) based on the density-insensitive ratio of $\text{N III}]\lambda 1750/\text{O III}]\lambda\lambda 1661, 1666$.

For the remaining 8 NOEGs where the abundances are derived from the optical lines including [N II] and [O II], N/O would be overestimated if the electron density reaches $n_e > 10^3 \text{ cm}^{-3}$ while a low density of $n_e < 10^3 \text{ cm}^{-3}$ is assumed. For 5 of such NOEGs reported by Stiavelli et al. (2025), 3 of them have electron densities derived from $[\text{S II}]\lambda\lambda 6716, 6730$, which in principle probe a similar density zone as $[\text{O II}]\lambda\lambda 3726, 3729$. The NOEGs reported by Zhang et al. (2025) and Arellano-Córdova et al. (2025) also have low-ionization zone densities. Therefore, only two NOEGs, ID1477 and ID397 in our sample do not have density constraints for their optical-line based N/O. The above results suggest little impact from density variations for most of NOEGs in our sample.

Next, we comment on the potential impact of temperature inhomogeneity. Naively, emission lines from highly ionized species are in high-ionization zones that are closer to the ionizing source, implying a higher emissivity-weighted temperature compared to the lines in low-ionization zones. Such a temperature gradient would enhance N IV] and C IV relative to N III] and O III] at fixed N/O and C/O compared to the case where the temperature is uniform, leading to overestimations of the abundance ratios if one uses the temperature of O²⁺ derived from $[\text{O III}]\lambda 4363/[\text{O III}]\lambda 5007$ (Ji et al. 2024). It is thus useful to use a higher temperature for higher ionization species by using, for example, photoionization models (Ji et al. 2024). Still, abundance ratios inferred from $\text{N III}]\lambda 1750/\text{O III}]\lambda\lambda 1661, 1666$ or $\text{C III}]\lambda\lambda 1906, 1908/\text{O III}]\lambda\lambda 1661, 1666$ should be relatively robust as N²⁺, C²⁺, and O²⁺ share similar ionization potentials and should be spatially close. In addition, if high-ionization emission lines dominate the abundance derivation, one would expect C/O is also biased high as N/O, which is not commonly seen in NOEGs. As an example, among the 22 NOEGs we compiled, 14 have their N/O derived from UV semi-forbidden transitions, whereas only one source, GN-z9p4, has its N/O determined through N IV] and O III] due to the non-detection of N III] (Schaerer et al. 2024).

Finally, we note that there is an alternative explanation for the seemingly high N/O in NOEGs recently proposed by Flury et al. (2025), who suggested prevalent ionization by slow/intermediate-velocity radiative shock in the early Universe that biases the abundance derivation usually based on assumptions of photoionization. However, shock models rely on additional assumptions due to the intrinsically high dimensionality of their parameter space (e.g., shock velocity and magnetic field strength in addition to the typical parameters assumed for photoionization models). Also, as shown by Flury et al. (2025), with their shock models, nitrogen enhancement for sources such as GS_3073 and GN-z11 is reduced, but not removed compared to local galaxies. Detailed comparisons between the nebular properties of NOEGs and shocked dominated nebulae in the local Universe will be important to further test this scenario.

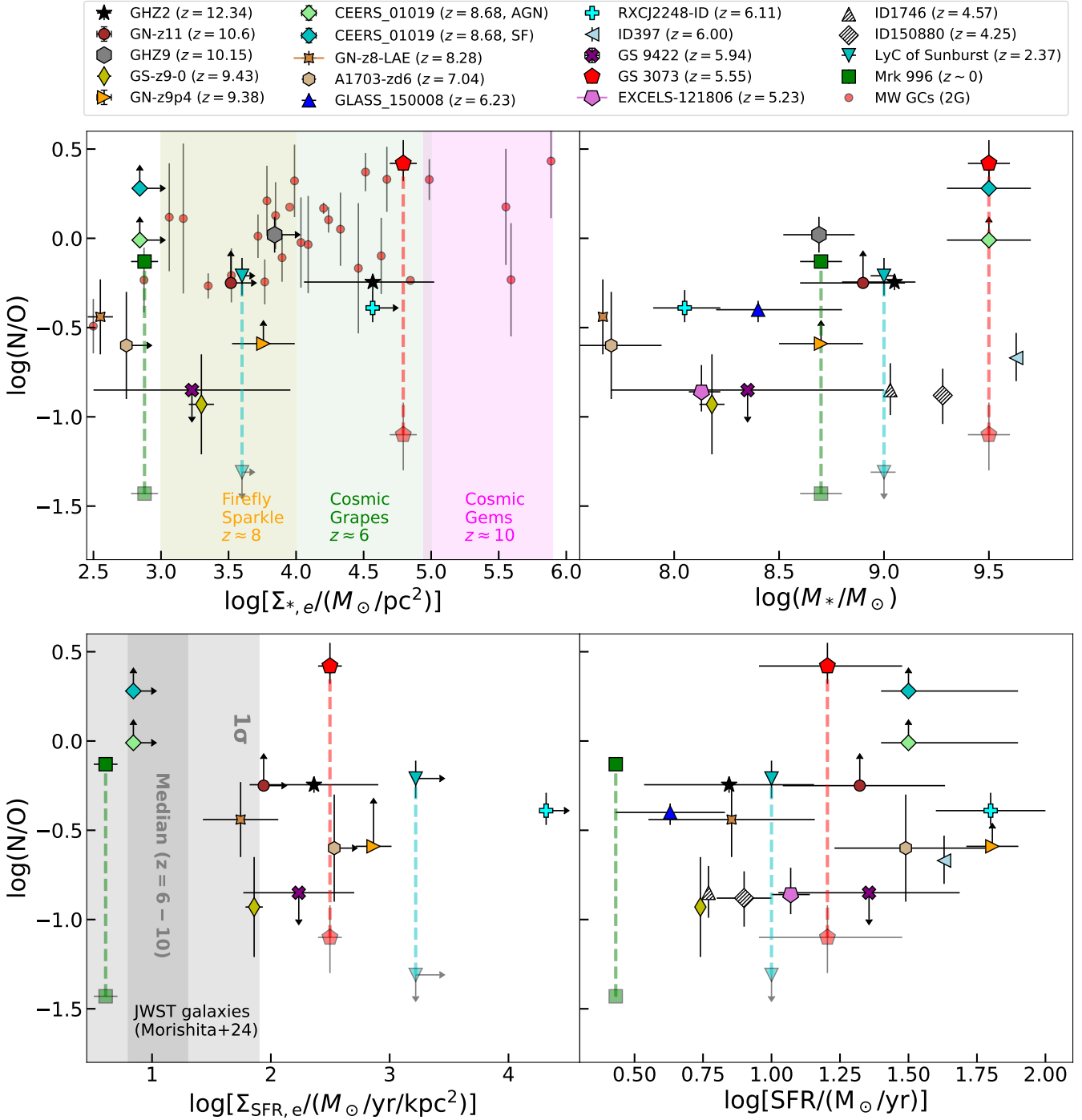


Figure 6. *Top:* Stellar masses and stellar mass surface densities versus N/O for the sample of NOEGs. For systems showing two N/O values connected by dashed lines, the higher values correspond to high-density components and lower values correspond to low-density components. Overall, NOEGs have high stellar mass surface densities of $\Sigma_{*,e} \gtrsim 10^{2.5} M_\odot \text{ pc}^{-2}$ consistent with progenitor environments of MW GCs and star clusters observed in lensed galaxies shown as shaded regions (Vanzella et al. 2023; Fujimoto et al. 2025; Mowla et al. 2024; Adamo et al. 2024). While there is no clear correlation between N/O and stellar mass surface density, in most systems the effective radius, R_e , is not well constrained (see Table 1). In comparison, we also plot the distribution of MW GCs (small red dots), where we approximate their initial stellar mass surface density with the current-day projected core density (see text). The N/O ratios for GCs are median values among 2G stars and the errorbars correspond to the standard deviations. The GCs occupy a similar parameter space as NOEGs, although we note that the actual initial densities of GCs could be different due to mass segregation as GCs evolve. In the right panel, the N/O enhancement in NOEGs potentially shows a positive correlation with the total stellar mass of their hosts. *Bottom:* SFR and SFR surface densities versus N/O for NOEGs. In comparison, the median SFR surface densities of JWST galaxies (binned at median photometric redshifts of $z_{\text{photo}} = 6, 8$, and 10) compiled by Morishita et al. (2024) along with the 1σ dispersion are shown as the gray shaded region. The NOEGs are generally actively star-forming and have SFR surface densities higher than typical high- z galaxies.

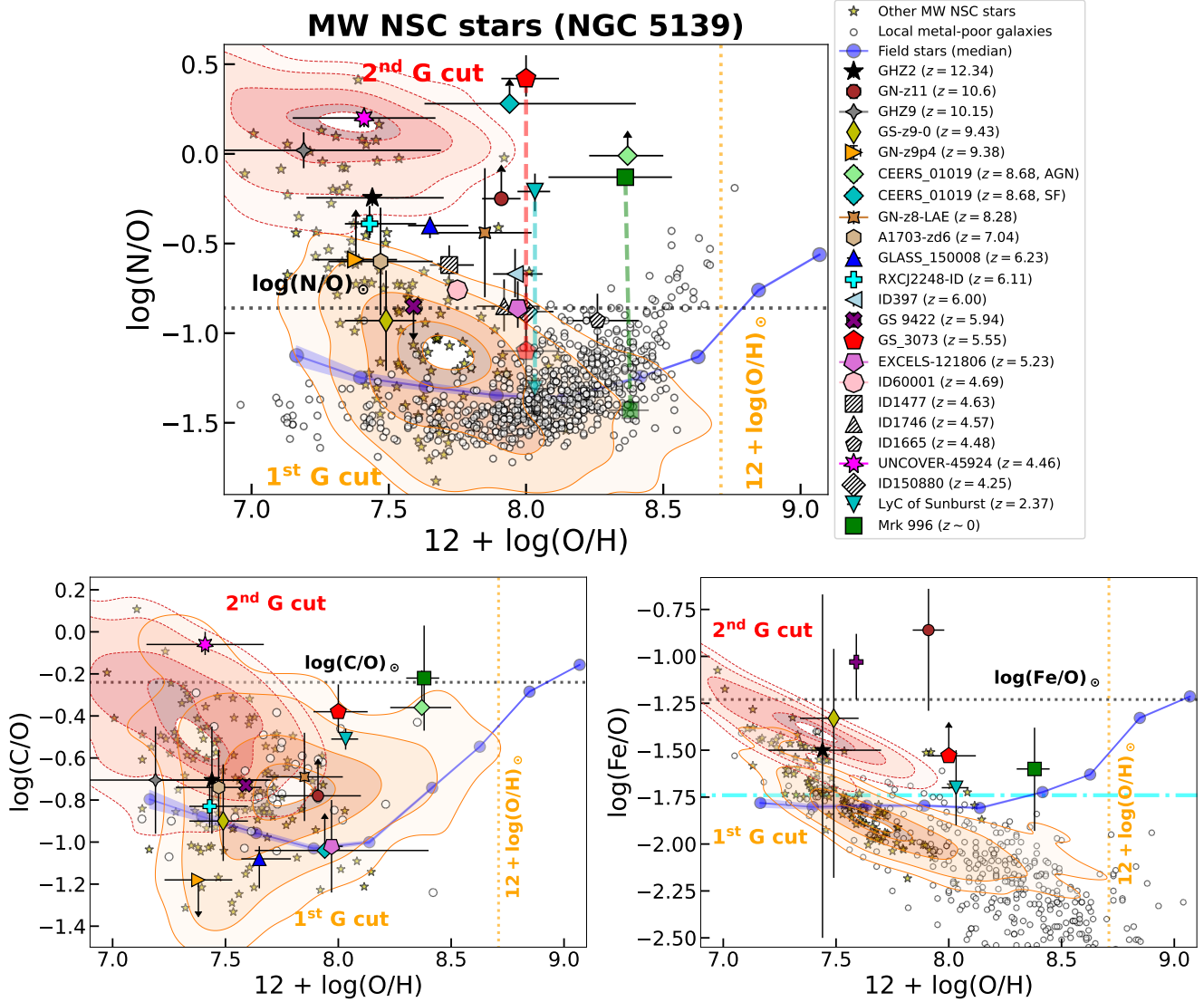


Figure 7. Same as Figures 2, 3, and 4, but the MW GC stars are replaced with those likely previously associated with NSCs of dwarf galaxies. These include NGC 5139, NGC 6273, NGC 6656, and NGC 1851 (Pfeffer et al. 2021; McKenzie et al. 2022). Since NGC 5139 dominates the distribution, we plot it as colored contours and plot the other NSC stars as yellow star symbols. While NSCs typically have multiple stellar populations, for illustrative purposes, we apply the same cut as we did for GCs to separate the “first generation” from the “second generation”, which should only be considered as a rough cut in formation time. The NSCs show stronger enhancement in N/O and C/O at lower O/H compared to typical GCs, which potentially arise from their extended star-formation history. This makes NSC abundances better match the NOEG UNCOVER-45924, which has potentially enhanced N/O and C/O in its BLR.

In summary, current observational evidence suggests that there are complex environments in NOEGs with varying densities and temperatures. Still, current estimations of the abundance patterns of N/O and C/O for the majority of NOEGs are unlikely to be significantly biased.

5.2 Environments of the abundance anomalies

One avenue to investigate the origin of NOEGs is to identify correlations between nitrogen enhancement and other galaxy properties. We note that due to the heterogeneous selection of NOEGs from samples with complex selection functions, we do not attempt to quantify the statistical occurrence rate of NOEGs, but rather perform a qualitative assessment of the derived properties among NOEGs.

5.2.1 Compactness

Perhaps the most common feature of NOEGs is the compactness of these systems, where the presence of a component with $R_e < 200$ pc is usually seen (see Table 1 and Figure 1). This makes NOEGs much more compact compared to other UV-bright galaxies with $R_e \sim 1$ kpc at $z \sim 4$ and $R_e \sim 0.3 - 0.6$ kpc at $z \sim 10$ (Shibuya et al. 2015; Harikane et al. 2025). In the left panel of Figure 6, we plot N/O as a function of the average stellar mass surface density within the effective radius for NOEGs in our sample. While there is no clear correlation between N/O and $\Sigma_{\star, e}$ (given the loose constraints on R_e), the stellar populations in NOEGs are overall densely distributed with $\Sigma_{\star, e} \gtrsim 10^{2.5} M_{\odot} \text{ pc}^{-2}$. Such a dense environment is again in good agreement with those inferred for the local GCs. For example, the progenitor gas environment of MW GCs likely has a gas mass density of $\Sigma_{\text{gas}} \sim 10^3 M_{\odot} \text{ pc}^{-2}$ (Gieles et al. 2025). We performed another

Table 3. Summary of the physical properties of star clusters observed in gravitationally lensed galaxies at high redshift. The 1σ relative measurement uncertainty in the total lensing magnification, μ , varies among galaxies from as low as 3% to 20-50%, with systematic uncertainties due to lensing models potentially reaching 50% and higher. However, since M_\star (at fixed M/L) roughly scales linearly with μ^{-1} and R_e ; intrinsic roughly scales linearly with $\mu^{-0.5}$, the stellar mass surface density is less affected by the uncertainty in the lensing magnification.

Name	z	$N_{\text{cluster, identified}}$	μ	R_e ; intrinsic [pc]	$\log \Sigma_{\star, e}$; intrinsic [$M_\odot \text{ pc}^{-2}$]
Sunburst Arc ^a	2.37	15	15 - 484	0.9 - 23.7	3 - 4
Sunrise Arc ^b	6.0	6	$\gtrsim 30 - 66$	1.4 - 24.8	3 - 5
Cosmic Grapes ^c	6.07	15	22 - 43	7 - 62	3 - 5
Firefly Sparkle ^d	8.30	10	16 - 26	$< 4 - 7$	$> 3 - 4$
Cosmic Gems ^e	10.2	5	57 - 420	0.7 - 1	5 - 6

Notes. References: ^a [Vanzella et al. \(2022\)](#); ^b [Vanzella et al. \(2023\)](#); ^c [Fujimoto et al. \(2025\)](#); ^d [Mowla et al. \(2024\)](#); ^e [Adamo et al. \(2024\)](#).

calculation to estimate the initial stellar mass surface density of MW GCs. Specifically, we took the core densities (ρ_c) and radii (r_c) of MW GCs fitted by [Baumgardt & Hilker \(2018\)](#). Simply assuming a constant density in the core, the average surface mass density of the core is $\Sigma_c = \frac{4\pi}{3} r_c^3 \rho_c / (\pi r_c^2) = \frac{4}{3} \rho_c r_c$. Then, if we approximate the initial densities of GCs with the current-day core densities (which is not exact due to mass segregation as GCs evolve, [Fregeau et al. 2002](#)), we obtained a median surface density of $\Sigma_{\text{ini, GC}} \approx 4 \times 10^3 M_\odot \text{ pc}^{-2}$, comparable with the densities seen in NOEGs. We further plotted estimated $\Sigma_{\text{ini, GC}}$ and median N/O of 2G stars for individual GCs in the left panel of Figure 6, where one can see a good overlap between GCs and NOEGs in terms of their compact stellar populations and N/O enhancement. In the early time of the evolution of the MW, star formation is likely not dominated by a smooth disk component but rather by dense star clusters in a turbulent environment ([Belokurov & Kravtsov 2022, 2023](#)). Such an early phase of cluster-dominated evolution might be common in *JWST*-observed high- z systems, which is evident from the dense environments seen in NOEGs.

Observations of highly gravitationally lensed galaxies also provide direct evidence for cluster-dominated star formation at high redshift ([Vanzella et al. 2022, 2023; Mowla et al. 2024; Fujimoto et al. 2025; Adamo et al. 2024](#)). In Table 3, we summarize derived properties of observed lensed galaxies at high redshift, where individual SF clumps were identified and proposed as proto-GC candidates. For example, [Vanzella et al. \(2023\)](#) reported observations of 6 star clusters by *JWST*/NIRCam in the highly magnified galaxy, the Sunrise Arc, at $z \sim 6$. These clusters have a range of stellar mass surface densities of $\Sigma_{\star, e} = 10^{3-5} M_\odot \text{ pc}^{-2}$ and contribute to 10 - 30% of the recently formed stellar mass in this galaxy. As another example, [Fujimoto et al. \(2025\)](#) reported a lensed galaxy, the Cosmic Grapes, at $z = 6.072$, where at least 15 star clusters with $\Sigma_{\star, e} = 10^{3-5} M_\odot \text{ pc}^{-2}$ are identified. These star clusters make up of 70% of the stellar mass of the whole galaxy. Notably, in the integrated *JWST*/NIRSpec IFU spectrum of the Cosmic Grapes, [Fujimoto et al. \(2025\)](#) found significant detection of $[\text{N II}]\lambda 6583$ and $[\text{O II}]\lambda\lambda 3726, 3729$, and they derived a normal $\log(\text{N/O}) = -1.46 \pm 0.04$ at $12 + \log(\text{O/H}) = 8.11 \pm 0.03$, which is in good agreement with the local scaling relation. This result seems to suggest no N/O enhancement in these star clusters, although we note that N/O enhancement in the rest-frame UV cannot be completely ruled out, as seen in some of the NOEGs shown in Figure 2, where N/O inferred from optical lines are consistent with the local scaling relation. At $z = 8.304$, [Mowla et al. \(2024\)](#) reported a gravitationally lensed galaxy, the Firefly Sparkle, where 10 star clusters are identified. These star clusters have stellar mass surface densities of $\Sigma_{\star, e} = 10^{3-4} M_\odot \text{ pc}^{-2}$, consistent with the expected densities of progenitors of the MW GCs. Also, [Mowla et al. \(2024\)](#) show that roughly 50% of the stellar mass in the Firefly Sparkle is within the 10 star clusters, supporting the scenario of cluster-dominated star formation. Unfortunately, there is no coverage of the

optical $[\text{N II}]\lambda 6583$ line in the *JWST*/NIRSpec spectrum and there is no detection of any UV nitrogen lines to constrain N/O. Finally, there is a lensed galaxy, the Cosmic Gems Arc, reported by [Adamo et al. \(2024\)](#) at $z = 10.2$ with 5 extremely dense star clusters making up 15 - 35% of the total stellar mass, although no spectrum is available to verify whether they exhibit any level of nitrogen enhancement.

In the top left panel of Figure 6, we also show the ranges of the surface mass densities of the star clusters observed in the above high-redshift galaxies. There is clearly a wide range of cluster densities in the early Universe, which covers the range of stellar densities seen in NOEGs. If we exclude UNCOVER-45924, whose stellar mass might have a large systematic uncertainty due to the spectral decomposition, GS_3073 exhibits the highest stellar mass density and the highest N/O at the same time. The extremely dense environments could help produce the extreme nitrogen enhancement according to enrichment channels such as VMSs, EMSs, and SMSs, where the high density is a necessary condition (e.g., to allow for rapid formation via inertial flows or stellar collisions; [Gieles et al. 2025](#)). Additionally, the dense environments could help to maintain the enriched light elements, which would also imply concentration of the abnormal abundances on cluster scales. Such a spatially confined enrichment is also supported by the three NOEGs showing two abundance patterns, which are the Mrk 996, LyC, and GS_3073, as noted by [Ji et al. \(2024\)](#). As a rough estimation, if one takes a minimum gas density of $n_H = 10^5 \text{ cm}^{-3}$ as the condition for N/O enhancement, as seen in the three NOEGs, the corresponding hydrogen mass density is $\rho_H = n_H m_H \approx 2.5 \times 10^3 M_\odot \text{ pc}^{-3}$, comparable to the median core density of MW GCs seen today, which is $\rho_c, \text{med} \approx 3.5 \times 10^3 M_\odot \text{ pc}^{-3}$ based on the measurements of [Baumgardt & Hilker \(2018\)](#). The similar values of densities, although not directly related, further indicate cluster-scale enrichment seen in NOEGs.

In addition to the stellar mass surface density, the compactness of NOEGs is also reflected by their star-formation rate (SFR) surface density. We compiled measurements of total SFRs reported by the literature listed in Table 1 for NOEGs and calculated $\Sigma_{\text{SFR, e}} = \text{SFR} / (2\pi R_e^2)$. Most of the SFRs are estimated through SED fitting (sometimes in combination with $\text{H}\alpha$ luminosities). For the unobscured AGN host GS_3073, we adopted the SFR estimated from $[\text{C II}]\lambda 158\mu\text{m}$ by [Übler et al. \(2023\)](#) to reduce the AGN contamination, which is much lower than the value obtained through SED fitting. In the bottom left panel of Figure 6, we plot SFR surface densities versus N/O for NOEGs that have SFR estimates. Clearly, most NOEGs are very compact SF systems compared to typical galaxies observed at high redshift, as noted by [Schaerer et al. \(2024\)](#). In fact, these NOEGs have higher SFR surface densities compared to the most intense starburst galaxies in the local Universe ([Kennicutt 1998; Bigiel et al. 2008](#)). Previous observational and theoretical works have shown an increase in the efficiency of forming bound clusters as the SFR surface density increases (e.g., [Adamo et al.](#)

2011, 2015; Kruijssen 2012). Thus, the high SFR surface densities of NOEGs are consistent with the picture that they are efficiently forming proto-GCs.

It will thus be informative for future work to compare chemical enrichment in dense star clusters and diffuse ISM at high redshift, preferably in a sample of galaxies with spatially separated star clusters. Notably, the compact morphologies are also frequently seen in *JWST*-discovered AGN (e.g., Matthee et al. 2024; Maiolino et al. 2024b; Juodžbalis et al. 2025) and the coevolution of star clusters and AGN in the gas-rich environments in the early Universe are indeed expected (Neumayer et al. 2020). Next, we discuss the potential connection between NOEGs and actively accreting black holes.

5.2.2 Presence of accreting black holes

Recently, Isobe et al. (2025b) identified a potential connection between AGN activity and N/O enhancement by finding a relative enhancement of the nitrogen line, $\text{N}\text{III}\lambda 1750$, in a stack of Type 1 AGN in JADES at $4 < z < 7$. While the nitrogen lines can be enhanced by the presence of broad lines, Isobe et al. (2025b) argue that an enhancement in N/O must also exist to explain the difference between the stacked Type 1 AGN and SF galaxies. Among the 22 NOEGs we compiled, two are unambiguous Type 1 AGN (GS_3073, UNCOVER-45924), and six have AGN signatures (GS_9422, CEERS_01019, GS-z9-0, GHZ9, GN-z11, and GHZ2) indicated by high-ionization lines. Interestingly, in the pre-*JWST* era, a subclass of QSOs known as “nitrogen-loud QSOs” has been observed, which shows enhanced nitrogen lines in the UV, implying a high N/O (Baldwin et al. 2003). The population of the nitrogen-loud QSOs is very rare, comprising only 1% of QSOs from SDSS at $1.6 < z < 4$ (Bentz & Osmer 2004; Bentz et al. 2004; Jiang et al. 2008). For unobscured AGN and nitrogen-loud QSOs, specifically, it has been long speculated that the nitrogen enhancement is limited to the nuclear region where a past starburst produces the current chemical imprint (Hamann & Ferland 1993; Baldwin et al. 2003). The nuclear chemical imprints can be more easily seen once the dust is cleared out by feedback and the central black hole reaches the active accretion phase (Hamann & Ferland 1999). This points to chemical anomalies potentially dominated by NSCs, whose gravitational potential is deep enough to maintain the enriched gas. The early formation of NSCs could also seed massive black holes (Neumayer et al. 2020; Isobe et al. 2025b; Partmann et al. 2025; Vergara et al. 2025; Paiella et al. 2025), which might explain the “overmassive” black holes compared to the stellar masses of host galaxies seen in many high- z AGN discovered by *JWST* (e.g., Harikane et al. 2023; Übler et al. 2023; Maiolino et al. 2024b; Juodžbalis et al. 2025). Alternatively, some models suggest that extremely small-scale enrichment can occur in the extension of the accretion disk, where star formation can occur to produce abundance patterns with enhanced light elements for the BLR (e.g., Huang et al. 2023).

While the high- z AGN hosts might be more N/O enhanced compared to the non-AGN hosts as shown by Isobe et al. (2025b) and from Figure 2 focusing on GS_3073 and UNCOVER-45924, this should not be simply interpreted as a causality, and one needs to examine other physical properties as well. Notably, the duration of a single actively accreting phase of AGN ($\sim 0.1 - 100$ Myr; Morganti 2017) is comparable to the time scale of early enrichment by AGB stars ($\sim 40 - 300$ Myr; D’Antona et al. 2023) and those from other mechanisms (e.g., WRs, VMSs, EMSs, and SMSs; Watanabe et al. 2024; Vink 2023; Gieles et al. 2025; Charbonnel et al. 2023; Nandal et al. 2024a, 2025), and one possibility is the synchronization of AGN activities and nuclear star formation (Hamann & Ferland

1993). Still, a comparably large fraction of NOEGs in our sample do not show clear AGN signatures.

Since AGN activities are more frequently seen in more massive galaxies, one might wonder whether nitrogen enhancement in AGN hosts is actually a reflection of the mass dependence. In the top right panel of Figure 6, we plot N/O as a function of stellar masses of NOEGs. Interestingly, if we ignore the low-density components of some NOEGs (plotted as transparent symbols), there appears to be a positive trend where more massive galaxies are more N/O enhanced. The unobscured AGN host, GS_3073 ($z = 5.55$), is among both the most massive NOEGs and the most nitrogen enhanced NOEGs. The other unobscured AGN, UNCOVER-45924 ($z = 4.46$), is reported to be extremely massive with $\log M_\star/M_\odot = 10.9 \pm 0.2$ by Labb   et al. (2024). However, recent works have suggested the stellar mass estimates for the red compact AGN hosts with flat UV slopes and strong Balmer breaks (i.e., the “little red dots”; Matthee et al. 2024) such as UNCOVER-45924 are significantly overestimated due to the incorrect AGN decomposition in their spectra (Inayoshi & Maiolino 2025; Ji et al. 2025a; de Graaff et al. 2025; Naidu et al. 2025; Taylor et al. 2025). Thus, we did not adopt the current stellar mass estimate for this source. There are three sources, ID1746, ID150880, and ID397, having stellar masses of $10^{9-9.5} M_\odot$ and yet not significantly more enhanced N/O. However, from Figure 2, one can see these sources do not deviate strongly from the local scaling relations compared to many other NOEGs. One might wonder whether the tentative N/O- M_\star trend is driven by the mass-metallicity relation. Compared to what is shown in Figure 2, it is clear that the increased N/O is *not* driven by the increased O/H. In fact, there is instead anticorrelation between N/O and O/H at $12 + \log(\text{O/H}) < 8.0$, which is also seen in local GC stars and is explained by the enrichment of the 1G stars. Instead, if we look into the dependence of N/O on the SFR in the bottom right panel of Figure 6, there is a tentative positive trend, although with a large scatter similar to the N/O- M_\star trend. Regardless, both trends seem to suggest some global regulation of the N/O anomaly seen in NOEGs.

Finally, we note that the high-mass end of NOEGs might provide some insights into cluster-dominated star formation in early galaxies. In the MW, the *Aurora* stars formed before the emergence of the disk, which show strong evidence for a cluster-dominated mode of star formation. Studies by Belokurov & Kravtsov (2022, 2023) have demonstrated that *Aurora* stars exhibit abundance patterns characteristic of GCs and suggest a high fraction of stars formed in bound clusters. Importantly, Belokurov & Kravtsov (2023) estimate the total stellar mass of *Aurora* to be $\sim 10^9 M_\odot$, consistent with the stellar mass threshold for bursty, cluster-dominated star formation emerging from recent cosmological zoom-in simulations (e.g., Dillamore et al. 2024; Semenov et al. 2025). These simulations identify a critical halo mass of $\sim 10^{11} M_\odot$ corresponding to a critical stellar mass of a few $\times 10^9 M_\odot$, below which galaxies undergo bursty star formation, sustain high ambient pressures, and efficiently form long-lived bound clusters. Once above this threshold, galaxies develop stable disks, inflow becomes smooth, pressure drops, and the bound cluster formation efficiency falls by more than an order of magnitude within ~ 200 Myr.

This transition predicts that NOEGs, galaxies whose nebular gas already shows GC-like N/O enhancements, should be found primarily below this stellar mass threshold. However, the simulations underpinning this prediction are tailored to MW-mass progenitors, and their relevance to higher-mass systems is not guaranteed. If some NOEGs turn out to have significantly larger stellar or halo masses, they may lie outside the regime where such bursty, cluster-dominated formation is expected, and the current models may not apply. While current

JWST observations show NOEGs clustering at $M_\star \lesssim 10^{9.5} M_\odot$, this could partly reflect selection effects shown in Figure 1. Broader spectroscopic coverage across stellar mass will be needed to test whether the simulation-predicted threshold truly marks the end of GC-like star formation.

5.2.3 Connection to nuclear star clusters

Given the possible mass-N/O relation in NOEGs, one immediate question is whether the relation is physically expected. As we mentioned in Section 4.4, the fraction of galaxies hosting NSCs at $z \sim 0$ drops with stellar masses at $M_\star > 10^9 M_\odot$ (Neumayer et al. 2020), but it is nontrivial to trace it back to their progenitors, presumably the NOEGs except for the most massive ones that would involve into galaxies with $M_\star > 10^9 M_\odot$. In this case, taking GS_3073 as an example, its extreme N/O appears to contradict the expected low efficiency of NSC formation and growth, if one believes that the NSC is the key to driving the nitrogen enhancement in this scenario. However, as recently suggested by D’Antona et al. (2025), the nitrogen enhancement in GS_3073 could represent a snapshot during the evolution of a specific NSC, NGC 5139.

In Figure 7, we extract N/O and O/H of MW stars that are classified as NSCs of previous dwarf galaxies by Pfeffer et al. (2021); McKenzie et al. (2022). Since, in the APOGEE sample, 80% of the NSC stars come from a single NSC, NGC 5139, our comparison is essentially made between this NSC and NOEGs. We plot the stars in NGC 5139 as colored contours and the remaining NSC stars (from NGC 6273, NGC 6656, and NGC 1851) as scatter points. Although the overall distribution of stars in NGC 5139 (and other NSC stars) is broadly similar to that of general GC stars shown in Figure 2, they exhibit subtly but systematically different abundance patterns and are more strongly concentrated towards lower metallicities, with a clear paucity of stars at the metal-rich end. Since the statistics are dominated by NGC 5139, whether the mass scaling relation of NSC should drive the N/O- M_\star relation is unclear.

Regardless of any scaling relations associated with NSC formation, do we see direct evidence of such formation pathways in NOEGs? As shown in Figure 7, stars in NSCs—primarily from NGC 5139—exhibit systematically lower O/H, higher N/O, elevated C/O, and lower Fe/O relative to the general population of GC stars. These patterns have been reported in high-resolution spectroscopic studies of chemically complex clusters long suspected to be remnant NSCs (e.g., Smith et al. 2000; Yong et al. 2009; Marino et al. 2011, 2012; Yong et al. 2015). In these systems, carbon enhancement is found to correlate with *s*-process element enrichment, which is a signature of pollution by low-mass AGB stars. Because AGB winds are slow ($\leq 25 \text{ km s}^{-1}$) compared to energetic SN II ejecta, they can be retained within the cluster’s potential well and later recycled into subsequent stellar generations. However, the characteristic lifetimes of these low-mass polluters ($M < 3 M_\odot$) are ~ 300 Myr, requiring an extended star formation period that is only feasible in the deep potentials of NSCs.

In summary, low-mass AGB wind retention is not a generic feature of globular clusters. It requires exceptional gravitational binding to maintain the prolonged star formation that typifies nuclear star clusters or massive cluster complexes embedded in dwarf galaxy nuclei. Only in these environments can slow, carbon-rich AGB winds be retained while fast, oxygen-rich supernova ejecta escape—producing the elevated C/O that distinguishes NSC-type clusters from ordinary GCs. This elevated C/O is particularly noteworthy given its apparent similarity to that observed in the unobscured AGN host UNCOVER-45924. The chemical abundance pattern in UNCOVER-45924 thus

raises the intriguing possibility that it harbors not only an accreting supermassive black hole but also an emerging or fully formed NSC. Confirming this connection will require follow-up observations at higher spectral resolution to reduce systematic uncertainties in the derived abundances.

6 CONCLUSIONS

In this work, we investigated the connection between a sample of 22 “N/O-enhanced” galaxies (NOEGs) with enhanced nitrogen-to-oxygen ratios (i.e., super-solar N/O at sub-solar O/H) in their interstellar medium (ISM) at $0 \lesssim z \lesssim 12$ with field stars and globular cluster (GC) stars in the Milky Way (MW) through their chemical abundance patterns, including O/H, N/O, C/O, Fe/O, and He/H. These abundances trace different chemical enrichment mechanisms and time scales. We assume that the chemical abundances measured in the atmospheres of evolved MW stars capture the chemical composition of the ISM of their host galaxies at the time of formation. We summarize our conclusions below.

- The NOEGs occupy a unique parameter space in the N/O versus O/H diagram, where MW disk stars are rarely populated but MW stars in GCs including accreted nuclear star clusters (NSCs) candidates are commonly found (Figure 2). At low metallicities ($12 + \log(\text{O/H}) < 8.0$), currently discovered NOEGs show a tentative anticorrelation between N/O and O/H also present in GCs, which, for GC stars, is usually interpreted as evidence of oxygen depletion through the CNO cycle as GCs evolve and self-enrich the gas in the clusters. While there are also more metal rich NOEGs at $12 + \log(\text{O/H}) > 8.0$, they might still overlap with more metal-enriched GCs in the abundance space that are not representative in the MW GCs.
- In terms of the carbon abundance, NOEGs generally show sub-solar C/O consistent with either the low-metallicity MW field stars or GC stars (Figure 3). Only one NOEG, UNCOVER-45924 at $z = 4.46$, shows potentially super-solar C/O, which is more consistent with the abundance pattern of NSCs compared to GCs, although further observations are needed to verify this connection (Figure 7). The presence of an accreting supermassive black hole in this NOEG might point towards a coevolution scenario for the NSC and the black hole.
- In terms of the iron abundance, which is a typical tracer of a longer enrichment time scale, NOEGs exhibit a tentative anticorrelation between Fe/O and O/H similar to the trend observed in the ISM of local metal-poor galaxies and H II regions (Figure 4). This anticorrelation was previously interpreted as increased dust depletion with increased metallicity. While there is potential enhancement of Fe/O for NOEGs at low O/H reaching solar or super-solar Fe/O similar to the second generation GC stars, the measurements of Fe/O in these NOEGs are highly uncertain. Besides the depletion of oxygen via the CNO cycle, enhancement of Fe/O at low metallicities can also be caused by atypical supernova enrichment such as through the pair-instability supernovae or the hypernovae.
- The helium enhancement is found in both GC stars and potentially a few metal-poor NOEGs (Figure 5). Unlike previous work, we found no clear indication of any correlation between the helium enhancement and the N/O enhancement. However, there appears to be a tentative anticorrelation between the helium enhancement and the oxygen abundance in NOEGs. The enhancement of helium can either be interpreted as a bias induced by underestimated gas densities, suggested by the complicated density variations seen in some NOEGs, or a true enhancement caused by different initial masses of the proto-GCs involved. The latter interpretation implies more

massive proto-GCs or proto-NSCs found in the low metallicity environments with a longer enrichment time, which require further direct observational evidence from star clusters at high redshift to verify.

• Observations of NOEGs suggest a wide range of environments, which, however, share a common feature of high stellar densities consistent or higher than the expected progenitor environment of MW GCs and comparable to those directly observed in a few star clusters in high-redshift lensed galaxies (Figure 6). The dense environments would allow for the formation and growth of very-to-extremely massive stars ($M_\star \sim 10^2\text{--}10^4 M_\odot$), which is one of the proposed channels for producing the abundance anomalies in GCs and NOEGs. In addition, NOEGs predominantly show high star-formation rate surface densities, which might imply efficient formation of bound clusters. There is also evidence of accreting supermassive black holes in a few NOEGs (and, vice-versa, evidence for nitrogen enrichment in galaxies hosting accreting supermassive black holes found by JWST at high- z shown by previous work), indicating a possible connection from NOEGs and formation of black holes seeds (via collapses of very-to-extremely massive stars or runaway merging), as suggested by various models. Yet, the connection between the black hole accretion and nitrogen enhancement might also be caused by a common correlation with the stellar mass. There is a tentative N/O-stellar mass relation in NOEGs, where more massive NOEGs are more nitrogen enhanced, although verifications from a larger sample with quantified selection functions will be needed to verify the correlation.

As a concluding remark, the chemical similarities between local GCs and high-redshift NOEGs produce key evidence that connects the two populations. The seemingly high occurrence rates of NOEGs in the early Universe is qualitatively consistent with the picture of bursty, cluster-dominated star formation recently proposed for the early phase of galaxy evolution. Once galaxies transform from cluster-dominated star formation to disk-dominated star formation at later epochs, the chemical anomalies including the N/O enhancement in the ISM and later formed field stars should be erased and the former NOEGs would converge to the local scaling relations. While the above scenario is promising, we do note that there are alternative theories for massive cluster formation from, rather than prior to, the disk (e.g., Krumholz & Dekel 2010; Kruijssen 2012; Clarke et al. 2019). Future deep observations of a statistical sample of high-redshift galaxies with determinations of chemical abundances in spatially separated star clusters and inter-cluster regions will be important to further understand this connection.

ACKNOWLEDGEMENTS

We thank the anonymous referee, whose thoughtful comments improved the clarity of the this work. We thank Wyn Evans and Hui Li for helpful discussions. We thank Charlotte Simmonds for providing the photometric/spectroscopic catalogues of JADES galaxies. XJ and RM acknowledge ERC Advanced Grant 695671 “QUEENCH” and support by the Science and Technology Facilities Council (STFC) and by the UKRI Frontier Research grant RISEandFALL. VB acknowledges support from the Leverhulme Research Project Grant RPG-2021-205: “The Faint Universe Made Visible with Machine Learning”. RM acknowledges funding from a research professorship from the Royal Society. YI is supported by JSPS KAKENHI Grant No. 24KJ0202. AK was supported by the NASA ATP grant 80NSSC20K0512 and the National Science Foundation grant AST-2408267. HÜ acknowledges funding by the European Union (ERC APEX, 101164796). Views and opinions expressed are however those

of the authors only and do not necessarily reflect those of the European Union or the European Research Council Executive Agency. Neither the European Union nor the granting authority can be held responsible for them.

This work is based on observations made with the NASA/ESA/CSA James Webb Space Telescope. The data are available at the Mikulski Archive for Space Telescopes (MAST) at the Space Telescope Science Institute, which is operated by the Association of Universities for Research in Astronomy, Inc., under NASA contract NAS 5-03127 for JWST.

DATA AVAILABILITY

All JWST data used in this paper are available through the MAST portal. The APOGEE data are available through https://www.sdss4.org/dr17/data_access/. All analysis results of this paper will be shared on reasonable request to the corresponding author.

REFERENCES

Abdurro'uf et al., 2022, *ApJS*, **259**, 35
 Adamo A., Östlin G., Zackrisson E., 2011, *MNRAS*, **417**, 1904
 Adamo A., Kruijssen J. M. D., Bastian N., Silva-Villa E., Ryon J., 2015, *MNRAS*, **452**, 246
 Adamo A., et al., 2024, *Nature*, **632**, 513
 Allende Prieto C., Beers T. C., Wilhelm R., Newberg H. J., Rockosi C. M., Yanny B., Lee Y. S., 2006, *ApJ*, **636**, 804
 Alvarez Garay D. A., Mucciarelli A., Bellazzini M., Lardo C., Ventura P., 2024, *A&A*, **681**, A54
 Álvarez-Márquez J., et al., 2025, *A&A*, **695**, A250
 Amarsi A. M., Nissen P. E., Skúladóttir Á., 2019, *A&A*, **630**, A104
 Andrews B. H., Martini P., 2013, *ApJ*, **765**, 140
 Annibali F., et al., 2019, *MNRAS*, **482**, 3892
 Arellano-Córdova K. Z., et al., 2025, *MNRAS*, **540**, 2991
 Aver E., Olive K. A., Skillman E. D., 2015, *J. Cosmology Astropart. Phys.*, **2015**, 011
 Baldwin J. A., Hamann F., Korista K. T., Ferland G. J., Dietrich M., Warner C., 2003, *ApJ*, **583**, 649
 Bastian N., Lardo C., 2018, *ARA&A*, **56**, 83
 Baumgardt H., Hilker M., 2018, *MNRAS*, **478**, 1520
 Baumgardt H., Hilker M., Sollima A., Bellini A., 2019, *MNRAS*, **482**, 5138
 Belfiore F., et al., 2017, *MNRAS*, **469**, 151
 Belokurov V., Kravtsov A., 2022, *MNRAS*, **514**, 689
 Belokurov V., Kravtsov A., 2023, *MNRAS*, **525**, 4456
 Benjamin R. A., Skillman E. D., Smits D. P., 2002, *ApJ*, **569**, 288
 Bensby T., Feltzing S., Oey M. S., 2014, *A&A*, **562**, A71
 Bentz M. C., Osmer P. S., 2004, *AJ*, **127**, 576
 Bentz M. C., Hall P. B., Osmer P. S., 2004, *AJ*, **128**, 561
 Berg D. A., Skillman E. D., Henry R. B. C., Erb D. K., Carigi L., 2016, *ApJ*, **827**, 126
 Berg D. A., Erb D. K., Henry R. B. C., Skillman E. D., McQuinn K. B. W., 2019, *ApJ*, **874**, 93
 Bigiel F., Leroy A., Walter F., Brinks E., de Blok W. J. G., Madore B., Thornley M. D., 2008, *AJ*, **136**, 2846
 Böker T., et al., 2023, *PASP*, **135**, 038001
 Buder S., et al., 2025, *Publ. Astron. Soc. Australia*, **42**, e051
 Bunker A. J., et al., 2023, *A&A*, **677**, A88
 Bunker A. J., et al., 2024, *A&A*, **690**, A288
 Calabro A., et al., 2024, *ApJ*, **975**, 245
 Cameron A. J., Katz H., Rey M. P., Saxena A., 2023, *MNRAS*, **523**, 3516
 Cameron A. J., Katz H., Witten C., Saxena A., Laporte N., Bunker A. J., 2024, *MNRAS*, **534**, 523
 Caplar N., Tacchella S., 2019, *MNRAS*, **487**, 3845
 Carniani S., et al., 2025, *A&A*, **696**, A87

Carretta E., 2021, [A&A](#), **649**, A154

Castellano M., et al., 2024, [ApJ](#), **972**, 143

Charbonnel C., Schaefer D., Prantzos N., Ramírez-Galeano L., Frago T., Kuruvanthodi A., Marques-Chaves R., Gieles M., 2023, [A&A](#), **673**, L7

Clarke A. J., et al., 2019, [MNRAS](#), **484**, 3476

Cohen J. G., Kirby E. N., 2012, [ApJ](#), **760**, 86

Curti M., et al., 2025, [A&A](#), **697**, A89

D'Antona F., et al., 2023, [A&A](#), **680**, L19

D'Antona F., et al., 2025, [A&A](#), **700**, A265

D'Ercole A., Vesperini E., D'Antona F., McMillan S. L. W., Recchi S., 2008, [MNRAS](#), **391**, 825

D'Eugenio F., et al., 2024, [A&A](#), **689**, A152

D'Eugenio F., et al., 2025, [ApJS](#), **277**, 4

Del Zanna G., Dere K. P., Young P. R., Landi E., 2021, [ApJ](#), **909**, 38

Denissenkov P. A., Hartwick F. D. A., 2014, [MNRAS](#), **437**, L21

Dere K. P., Landi E., Mason H. E., Monsignori Fossi B. C., Young P. R., 1997, [A&AS](#), **125**, 149

Dillamore A. M., Belokurov V., Kravtsov A., Font A. S., 2024, [MNRAS](#), **527**, 7070

Dopita M. A., et al., 2006, [ApJ](#), **647**, 244

Dors O. L., Maiolino R., Cardaci M. V., Hägele G. F., Krabbe A. C., Pérez-Montero E., Armah M., 2020, [MNRAS](#), **496**, 3209

Eisenstein D. J., et al., 2023a, [arXiv e-prints](#), p. arXiv:2306.02465

Eisenstein D. J., et al., 2023b, [arXiv e-prints](#), p. arXiv:2310.12340

Ferland G. J., Hu C., Wang J.-M., Baldwin J. A., Porter R. L., van Hoof P. A. M., Williams R. J. R., 2009, [ApJ](#), **707**, L82

Ferland G. J., et al., 2017, [Rev. Mex. Astron. Astrofis.](#), **53**, 385

Ferruit P., et al., 2022, [A&A](#), **661**, A81

Flury S. R., Arellano-Córdova K. Z., Moran E. C., Einsig A., 2025, [MNRAS](#), **543**, 3367

Fregeau J. M., Joshi K. J., Portegies Zwart S. F., Rasio F. A., 2002, [ApJ](#), **570**, 171

Fujimoto S., et al., 2025, [Nature Astronomy](#)

Gaia Collaboration et al., 2021a, [A&A](#), **649**, A1

Gaia Collaboration et al., 2021b, [A&A](#), **649**, A1

García Pérez A. E., et al., 2016, [AJ](#), **151**, 144

Garnett D. R., Skillman E. D., Dufour R. J., Peimbert M., Torres-Peimbert S., Terlevich R., Terlevich E., Shields G. A., 1995, [ApJ](#), **443**, 64

Gieles M., Padoa P., Charbonnel C., Vink J. S., Ramírez-Galeano L., 2025, [MNRAS](#),

Gordon K. D., Clayton G. C., Misselt K. A., Landolt A. U., Wolff M. J., 2003, [ApJ](#), **594**, 279

Gratton R. G., et al., 2001, [A&A](#), **369**, 87

Gratton R., Sneden C., Carretta E., 2004, [ARA&A](#), **42**, 385

Gratton R., Bragaglia A., Carretta E., D'Orazi V., Lucatello S., Sollima A., 2019, [A&ARv](#), **27**, 8

Greggio L., Renzini A., 1983, [A&A](#), **118**, 217

Grossi M., et al., 2025, [arXiv e-prints](#), p. arXiv:2501.18498

Gunasekara C. M., Ji X., Chatzikos M., Yan R., Ferland G., 2023, [MNRAS](#), **520**, 4345

Hafen Z., et al., 2022, [MNRAS](#), **514**, 5056

Hamann F., Ferland G., 1993, [ApJ](#), **418**, 11

Hamann F., Ferland G., 1999, [ARA&A](#), **37**, 487

Harikane Y., et al., 2023, [ApJ](#), **959**, 39

Harikane Y., et al., 2025, [ApJ](#), **980**, 138

Hayden M. R., et al., 2015, [ApJ](#), **808**, 132

Hayes M. J., Saldana-Lopez A., Citro A., James B. L., Mingozi M., Scarlata C., Martinez Z., Berg D. A., 2025, [ApJ](#), **982**, 14

Haywood M., Di Matteo P., Lehnert M. D., Katz D., Gómez A., 2013, [A&A](#), **560**, A109

Henry R. B. C., Edmunds M. G., Köppen J., 2000, [ApJ](#), **541**, 660

Herwig F., 2004, [ApJS](#), **155**, 651

Hsyu T., Cooke R. J., Prochaska J. X., Bolte M., 2020, [ApJ](#), **896**, 77

Huang J., Lin D. N. C., Shields G., 2023, [MNRAS](#), **525**, 5702

Inayoshi K., Maiolino R., 2025, [ApJ](#), **980**, L27

Isobe Y., et al., 2022, [ApJ](#), **925**, 111

Isobe Y., et al., 2023, [ApJ](#), **959**, 100

Isobe Y., et al., 2025a, [arXiv e-prints](#), p. arXiv:2509.18055

Isobe Y., et al., 2025b, [MNRAS](#), **541**, L71

Izotov Y. I., Stasińska G., Meynet G., Guseva N. G., Thuan T. X., 2006, [A&A](#), **448**, 955

Izotov Y. I., Stasińska G., Guseva N. G., 2013, [A&A](#), **558**, A57

Izotov Y. I., Thuan T. X., Guseva N. G., 2014, [MNRAS](#), **445**, 778

Jakobsen P., et al., 2022, [A&A](#), **661**, A80

James B. L., Tsamis Y. G., Barlow M. J., Westmoquette M. S., Walsh J. R., Cuisinier F., Exter K. M., 2009, [MNRAS](#), **398**, 2

Jenkins E. B., 2009, [ApJ](#), **700**, 1299

Ji X., et al., 2024, [MNRAS](#), **535**, 881

Ji X., et al., 2025a, [MNRAS](#),

Ji X., et al., 2025b, [MNRAS](#), **541**, 2134

Jiang L., Fan X., Vestergaard M., 2008, [ApJ](#), **679**, 962

Jönsson H., et al., 2020, [AJ](#), **160**, 120

Juodžbalis I., et al., 2025, [arXiv e-prints](#), p. arXiv:2504.03551

Kane S. G., Belokurov V., Cranmer M., Monty S., Zhang H., Ardern-Arentsen A., 2025, [MNRAS](#), **536**, 2507

Karakas A., Lattanzio J. C., 2007, [Publ. Astron. Soc. Australia](#), **24**, 103

Kennicutt Jr. R. C., 1998, [ARA&A](#), **36**, 189

Kobayashi C., Karakas A. I., Lugaro M., 2020, [ApJ](#), **900**, 179

Kojima T., et al., 2021, [ApJ](#), **913**, 22

Kraft R. P., 1994, [PASP](#), **106**, 553

Kravtsov A., Belokurov V., 2024, [arXiv e-prints](#), p. arXiv:2405.04578

Krujissen J. M. D., 2012, [MNRAS](#), **426**, 3008

Krujissen J. M. D., 2015, [MNRAS](#), **454**, 1658

Krumholz M. R., Dekel A., 2010, [MNRAS](#), **406**, 112

Labbé I., et al., 2024, [arXiv e-prints](#), p. arXiv:2412.04557

Landi E., Young P. R., Dere K. P., Del Zanna G., Mason H. E., 2013, [ApJ](#), **763**, 86

Larson R. L., et al., 2023, [ApJ](#), **953**, L29

Leung H. W., Bovy J., 2019, [MNRAS](#), **489**, 2079

Lind K., Amarsi A. M., 2024, [ARA&A](#), **62**, 475

Lindegren L., et al., 2021, [A&A](#), **649**, A2

Lodders K., 2021, [Space Sci. Rev.](#), **217**, 44

Luridiana V., Morisset C., Shaw R. A., 2015, [A&A](#), **573**, A42

Mackereth J. T., Bovy J., 2018, [PASP](#), **130**, 114501

Maeder A., Meynet G., 2006, [A&A](#), **448**, L37

Maeder A., Meynet G., Chiappini C., 2015, [A&A](#), **576**, A56

Magrini L., et al., 2018, [A&A](#), **618**, A102

Maiolino R., Mannucci F., 2019, [A&ARv](#), **27**, 3

Maiolino R., et al., 2024a, [Nature](#), **627**, 59

Maiolino R., et al., 2024b, [A&A](#), **691**, A145

Maoz D., Mannucci F., 2012, [Publ. Astron. Soc. Australia](#), **29**, 447

Marino A. F., et al., 2011, [A&A](#), **532**, A8

Marino A. F., et al., 2012, [ApJ](#), **746**, 14

Marques-Chaves R., et al., 2024, [A&A](#), **681**, A30

Martinez Z., et al., 2025, [arXiv e-prints](#), p. arXiv:2510.21960

Matsumoto A., et al., 2022, [ApJ](#), **941**, 167

Matteucci F., 1986, [MNRAS](#), **221**, 911

Matteucci F., 2021, [A&ARv](#), **29**, 5

Matthee J., et al., 2024, [ApJ](#), **963**, 129

McClmont W., et al., 2025a, [arXiv e-prints](#), p. arXiv:2507.08787

McClmont W., et al., 2025b, [MNRAS](#), **544**, 513

McKenzie M., et al., 2022, [MNRAS](#), **516**, 3515

Méndez-Delgado J. E., et al., 2023, [MNRAS](#), **523**, 2952

Méndez-Delgado J. E., et al., 2024, [A&A](#), **690**, A248

Mészáros S., et al., 2020, [MNRAS](#), **492**, 1641

Meynet G., Maeder A., 2002, [A&A](#), **381**, L25

Milone A. P., Marino A. F., 2022, [Universe](#), **8**, 359

Milone A. P., et al., 2017, [MNRAS](#), **464**, 3636

Milone A. P., et al., 2018, [MNRAS](#), **481**, 5098

Minchev I., Chiappini C., Martig M., 2013, [A&A](#), **558**, A9

Morganti R., 2017, [Nature Astronomy](#), **1**, 596

Morishita T., et al., 2024, [ApJ](#), **963**, 9

Mowla L., et al., 2024, [Nature](#), **636**, 332

Mucciarelli A., Bellazzini M., Ibata R., Merle T., Chapman S. C., Dalessandro E., Sollima A., 2012, [MNRAS](#), **426**, 2889

Mucciarelli A., Bellazzini M., Merle T., Plez B., Dalessandro E., Ibata R., 2015, *ApJ*, **801**, 68

Nagele C., Umeda H., 2023, *ApJ*, **949**, L16

Naidu R. P., et al., 2025, arXiv e-prints, p. arXiv:2503.16596

Nakane M., et al., 2024, *ApJ*, **976**, 122

Nakane M., et al., 2025, arXiv e-prints, p. arXiv:2503.11457

Nandal D., Regan J. A., Woods T. E., Farrell E., Ekström S., Meynet G., 2024a, *A&A*, **683**, A156

Nandal D., Sibony Y., Tsatsi S., 2024b, *A&A*, **688**, A142

Nandal D., Whalen D. J., Latif M. A., Heger A., 2025, arXiv e-prints, p. arXiv:2502.04435

Napolitano L., et al., 2025, *ApJ*, **989**, 75

Navarro-Carrera R., Caputi K. I., Iani E., Rinaldi P., Kokorev V., Kerutt J., 2024, arXiv e-prints, p. arXiv:2407.14201

Neumayer N., Seth A., Böker T., 2020, *A&ARv*, **28**, 4

Nicholls D. C., Sutherland R. S., Dopita M. A., Kewley L. J., Groves B. A., 2017, *MNRAS*, **466**, 4403

Oliver K. A., Skillman E. D., 2004, *ApJ*, **617**, 29

Osterbrock D. E., Ferland G. J., 2006, Astrophysics of gaseous nebulae and active galactic nuclei

Paiella L., Arca Sedda M., Mestichelli B., Ugolini C., 2025, arXiv e-prints, p. arXiv:2511.00200

Partmann C., Naab T., Lahén N., Rantala A., Hirschmann M., Hislop J. M., Petersson J., Johansson P. H., 2025, *MNRAS*, **537**, 956

Pascale M., Dai L., McKee C. F., Tsang B. T. H., 2023, *ApJ*, **957**, 77

Peimbert M., 1967, *ApJ*, **150**, 825

Peimbert M., Peimbert A., Delgado-Ingla G., 2017, *PASP*, **129**, 082001

Pezzulli E., Valiante R., Orofino M. C., Schneider R., Gallerani S., Sbarato T., 2017, *MNRAS*, **466**, 2131

Pfeffer J., Lardo C., Bastian N., Saracino S., Kamann S., 2021, *MNRAS*, **500**, 2514

Pilyugin L. S., Grebel E. K., Mattsson L., 2012, *MNRAS*, **424**, 2316

Planck Collaboration et al., 2020, *A&A*, **641**, A6

Portegies Zwart S. F., McMillan S. L. W., Gieles M., 2010, *ARA&A*, **48**, 431

Prantzos N., Charbonnel C., 2006, *A&A*, **458**, 135

Prantzos N., Charbonnel C., Iliadis C., 2017, *A&A*, **608**, A28

Prantzos N., Abia C., Limongi M., Chieffi A., Cristallo S., 2018, *MNRAS*, **476**, 3432

Reina-Campos M., Kruijssen J. M. D., Pfeffer J., Bastian N., Crain R. A., 2018, *MNRAS*, **481**, 2851

Renzini A., 2025, *MNRAS*, **536**, L8

Rix H.-W., Bovy J., 2013, *A&ARv*, **21**, 61

Rizzuti F., Matteucci F., Molaro P., Cescutti G., Maiolino R., 2025, *A&A*, **697**, A96

Rodríguez M., Rubin R. H., 2005, *ApJ*, **626**, 900

Schaefer A. L., Tremonti C., Belfiore F., Pace Z., Bershady M. A., Andrews B. H., Drory N., 2020, *ApJ*, **890**, L3

Schaerer D., Marques-Chaves R., Xiao M., Korber D., 2024, *A&A*, **687**, L11

Schouws S., et al., 2025, *ApJ*, **988**, 19

Semenov V. A., Conroy C., Smith A., Puchwein E., Hernquist L., 2025, *ApJ*, **990**, 7

Senchyna P., Plat A., Stark D. P., Rudie G. C., Berg D., Charlot S., James B. L., Mingozi M., 2024, *ApJ*, **966**, 92

Sharon K., et al., 2022, *ApJ*, **941**, 203

Shibuya T., Ouchi M., Harikane Y., 2015, *ApJS*, **219**, 15

Simmonds C., et al., 2024, *MNRAS*, **535**, 2998

Smith G. H., 1987, *PASP*, **99**, 67

Smith V. V., Suntzeff N. B., Cunha K., Gallino R., Busso M., Lambert D. L., Straniero O., 2000, *AJ*, **119**, 1239

Stiavelli M., et al., 2025, *ApJ*, **981**, 136

Sun G., Faucher-Giguère C.-A., Hayward C. C., Shen X., 2023, *MNRAS*, **526**, 2665

Tacchella S., Forbes J. C., Caplar N., 2020, *MNRAS*, **497**, 698

Tacchella S., et al., 2023, *ApJ*, **952**, 74

Tacchella S., et al., 2025, *MNRAS*, **540**, 851

Tayal S. S., Zatsarinny O., 2017, *ApJ*, **850**, 147

Taylor A. J., et al., 2025, *ApJ*, **989**, L7

Table A1. Input parameters for CLOUDY photoionization models.

Parameter	Values
12 + log(O/H)	7.41
[N/O]	0.6, 0.7, 0.8, 0.9, 1.0, 1.1
[C/O]	-0.2, -0.1, 0, 0.1, 0.2, 0.3, 0.4
log U	-3.5, -3, -2.5, -2, -1.5, -1
log($n_{\text{H}}/\text{cm}^{-3}$)	9
log($N_{\text{H}}/\text{cm}^{-2}$)	23
AGN SED	$M_{\text{BH}} = 10^9 M_{\odot}$, $\lambda_{\text{Edd}} = 0.1$, 1 (Pezzulli et al. 2017)
Dust	No dust
Atomic data	CHIANTI (v7, Dere et al. 1997; Landi et al. 2013)

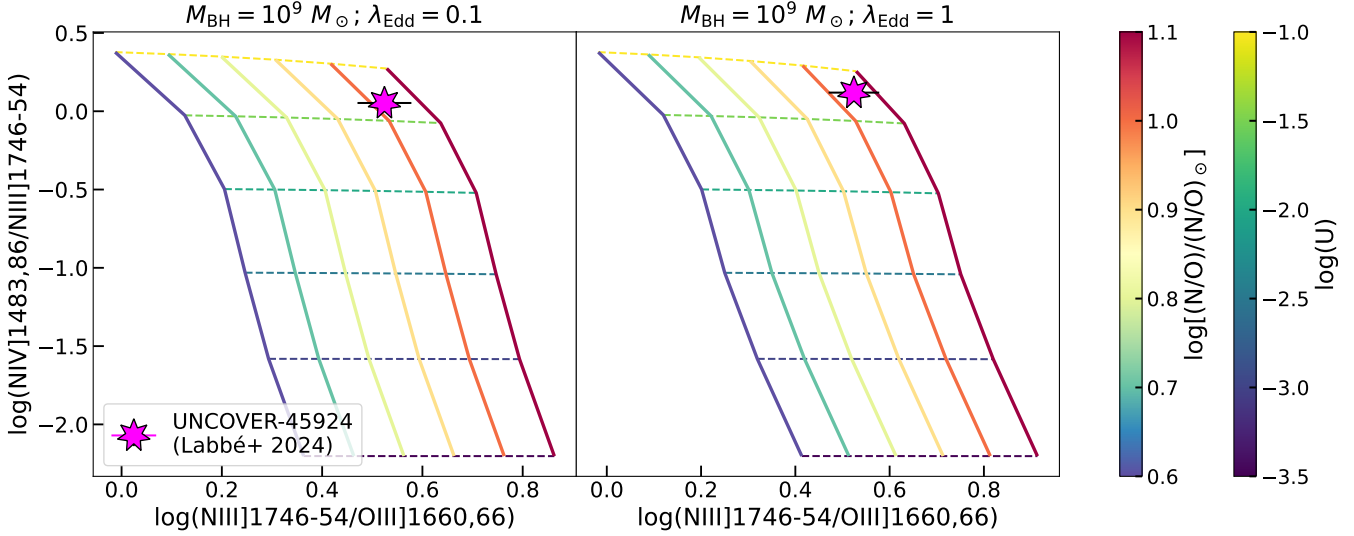


Figure A1. Comparison between observed line ratios of UNCOVER-45924 measured by Labb   et al. (2024) and those predicted by CLOUDY photoionization models, where all emission lines involved are assumed to come from a BLR cloud with $n_{\text{H}} = 10^9 \text{ cm}^{-3}$ and $N_{\text{H}} = 10^{23} \text{ cm}^{-2}$. The two panels show two sets of models with different Eddington ratios, λ_{Edd} . For each set of models, values of N/O and U are varied independently and $12 + \log(\text{O/H})$ is fixed to 7.41 (see Section 3). As shown by the models, the x axis, $\text{N III]}/\text{O III]}$, mainly traces N/O; the y axis, $\text{N IV]}/\text{N III]}$, mainly traces U. The best-fit model for UNCOVER-45924 has an N/O roughly 1 dex above solar.

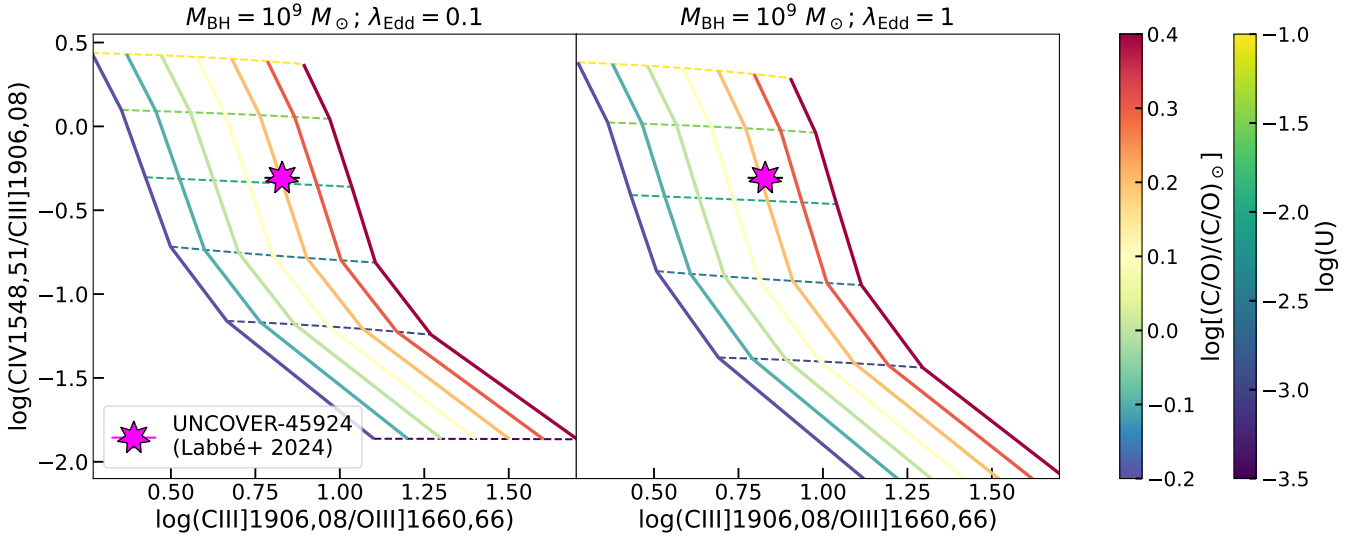


Figure A2. Comparison between observed line ratios of UNCOVER-45924 measured by Labb   et al. (2024) and those predicted by CLOUDY photoionization models, where all emission lines involved are assumed to come from a BLR cloud with $n_{\text{H}} = 10^9 \text{ cm}^{-3}$ and $N_{\text{H}} = 10^{23} \text{ cm}^{-2}$. The two panels show two sets of models with different Eddington ratios, λ_{Edd} . For each set of models, values of C/O and U are varied independently and $12 + \log(\text{O/H})$ is fixed to 7.41 (see Section 3). As shown by the models, the x axis, $\text{N III]}/\text{O III]}$, mainly traces N/O; the y axis, $\text{C IV}/\text{C III]}$, mainly traces U. The best-fit model for UNCOVER-45924 has an C/O roughly 0.2 dex above solar.

APPENDIX A: DERIVATION OF N/O AND C/O FOR UNCOVER-45924

In this appendix, we describe the derivation of N/O and C/O for UNCOVER-45924 (Labb   et al. 2024) based on CLOUDY (c17.03, Ferland et al. 2017) photoionization models. While we follow the argument of Labb   et al. (2024) to use BLR models to describe the relevant emission lines, if these lines actually come from an NLR with lower densities (i.e., $n_{\text{e}} < 10^8 \text{ cm}^{-3}$), the in-

ferred N/O is actually higher due to the density dependence of $\text{N III]}\lambda 1750/\text{O III]}\lambda\lambda 1661, 1666$. We summarize our fiducial model set in Table A1. The choice of $n_{\text{H}} = 10^9 \text{ cm}^{-3}$ is to obtain a conservative estimate of N/O. We set $N_{\text{H}} = 10^{23} \text{ cm}^{-2}$ as a typical value for BLR emission-line modeling (e.g., Ferland et al. 2009), and we note that higher column densities would not impact the results significantly as high ionization lines are mainly produced close to the illuminated face of the clouds (Ji et al. 2024). We allow the ionization

parameter to vary in a wide range reaching $\log(U) = -1$. We take the input AGN SED from the analytical model of [Pezzulli et al. \(2017\)](#), where we set a black hole mass of $10^9 M_\odot$ and two Eddington ratios ($\lambda_{\text{Edd}} \equiv L_{\text{bol}}/L_{\text{Edd}}$) of 0.1 and 1 possible for UNCOVER-45924 ([Labbé et al. 2024](#)). Finally, we assume the BLR is dust free.

Figures [A1](#) and [A2](#) show comparisons between line ratios measured by [Labbé et al. \(2024\)](#) corrected for dust extinction (see Section 3, although the corrections are modest due to the lines involved have similar wavelengths) and our model grids. In each diagram, the y axis is designed to trace the ionization parameter and the x axis is designed to trace mainly N/O or C/O at fixed O/H. From these two figures, UNCOVER-45924 exhibits a very high ionization parameter of $\log(U) = -2 - -1.25$. Ratios of N IV]/N III] and C IV/C III] give U values differ by 0.5 dex, which might be caused by a spatial stratification of different ionization species, an additional unresolved narrow component in N IV], or the radiative transfer of C IV. To estimate N/O and C/O, we interpolate models in the logarithm space of U and N/O (or C/O) with different λ_{Edd} using the `PYTHON` function `GRIDDATA` with a cubic spline function. We then search for the most likely model points for UNCOVER-45924 and take the average N/O (or C/O) of models with different λ_{Edd} , resulting in $\log(\text{N/O}) = 0.20^{+0.06}_{-0.05}$ and $\log(\text{C/O}) = -0.06^{+0.06}_{-0.05}$ with a systematic uncertainty of 0.10 dex from the different values of ionization parameters.

This paper has been typeset from a `TeX/LaTeX` file prepared by the author.